Cell Reports
Medicine

Article

Antitumor efficacy of a sequence-specific DNA-targeted γPNA-based *c-Myc* inhibitor

Graphical abstract

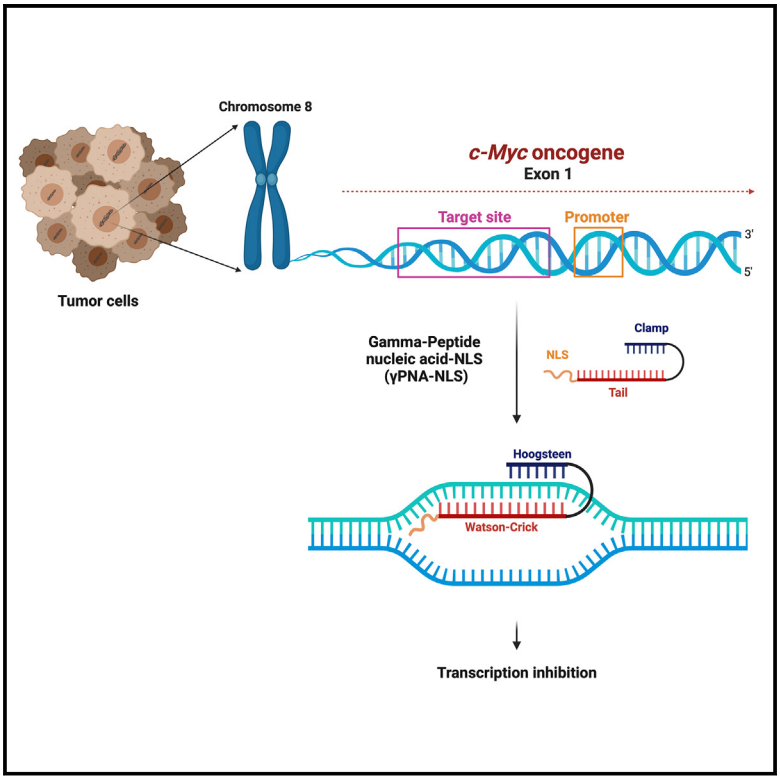

Highlights

- γPNA targets the genomic DNA sequence specifically to inhibit transcription *in vivo*
- γPNA-NLS inhibits the growth of tumors in multiple mouse models
- Efficacy of γPNA-NLS increases in combination with histone deacetylase inhibitors
- γPNA-NLS-mediated inhibition transcription sensitizes the tumor to chemotherapy

Authors

Shipra Malik, Sai Pallavi Pradeep, Vikas Kumar, ..., Juan C. Vasquez, Vijender Singh, Raman Bahal

Correspondence

raman.bahal@uconn.edu

In brief

Malik, Pradeep et al. utilize γPNA to target genomic DNA and silence *c-Myc* for cancer therapy. This DNA-targeting approach demonstrates high specificity and robust antitumor activity *in vivo*. The antigene γPNA in combination with HDACi and chemotherapy increases the anti-cancer efficacy, offering a promising avenue in precision medicine.

Malik et al., 2024, Cell Reports Medicine *5*, 101354
January 16, 2024
https://doi.org/10.1016/j.xcrm.2023.101354

CellPress

Cell Reports Medicine

CellPress
OPEN ACCESS

Article

Antitumor efficacy of a sequence-specific DNA-targeted γPNA-based *c-Myc* inhibitor

Shipra Malik,[1,9] Sai Pallavi Pradeep,[1,9] Vikas Kumar,[1] Yong Xiao,[2,3] Yanxiang Deng,[2,4] Rong Fan,[2,4,5,6] Juan C. Vasquez,[7] Vijender Singh,[8] and Raman Bahal[1,10,*]

[1]Department of Pharmaceutical Sciences, University of Connecticut, Storrs, CT 06269, USA
[2]Department of Biomedical Engineering, Yale University, New Haven, CT 06510, USA
[3]Department of Neurosurgery, Nanjing Brain Hospital Affiliated to Nanjing Medical University, Nanjing, China
[4]Yale Stem Cell Center and Yale Cancer Center, Yale School of Medicine, New Haven, CT 06520, USA
[5]Human and Translational Immunology, Yale School of Medicine, New Haven, CT 06520, USA
[6]Department of Pathology, Yale School of Medicine, New Haven, CT 06520, USA
[7]Department of Pediatrics, Yale School of Medicine, New Haven, CT 06520, USA
[8]Institute for Systems Genomics, University of Connecticut, Storrs, CT 06269, USA
[9]These authors contributed equally
[10]Lead contact
*Correspondence: raman.bahal@uconn.edu
https://doi.org/10.1016/j.xcrm.2023.101354

SUMMARY

Targeting oncogenes at the genomic DNA level can open new avenues for precision medicine. Significant efforts are ongoing to target oncogenes using RNA-targeted and protein-targeted platforms, but no progress has been made to target genomic DNA for cancer therapy. Here, we introduce a gamma peptide nucleic acid (γPNA)-based genomic DNA-targeted platform to silence oncogenes *in vivo*. γPNAs efficiently invade the mixed sequences of genomic DNA with high affinity and specificity. As a proof of concept, we establish that γPNA can inhibit *c-Myc* transcription in multiple cell lines. We evaluate the *in vivo* efficacy and safety of genomic DNA targeting in three pre-clinical models. We also establish that anti-transcription γPNA in combination with histone deacetylase inhibitors and chemotherapeutic drugs results in robust antitumor activity in cell-line- and patient-derived xenografts. Overall, this strategy offers a unique therapeutic platform to target genomic DNA to inhibit oncogenes for cancer therapy.

INTRODUCTION

The potential of targeting messenger RNA (mRNA) has been recognized with the approval of several RNA-targeted drugs (RTDs or antisense drugs) for treatment in the clinic.[1,2] However, RTDs have made limited progress in oncology-based therapeutics. Similarly, proteolysis-targeting chimeras (PROTACs) for targeted oncoprotein degradation have been used for prostate and breast cancer treatments.[3] Though promising, the mutations in the genomic DNA drive oncogenesis and its progression, which limits RTD- and PROTAC-based therapeutics. Targeting genomic DNA has been a long-term goal to control gene expression and treat diseases from the root level. Drugs like cisplatin, temozolomide, and cyclophosphamide target genomic DNA via intercalation to inhibit growth and proliferation of cancer cells.[4] However, these drugs cause severe toxicity by non-specifically targeting the genomic DNA in normal cells.[5,6] To address this, the focus shifted to developing reagents that can sequence-specifically target the genomic DNA via Watson-Crick (WC) base-pairing. Challenges in developing DNA-targeted therapies include accessing the DNA target site within chromatin,[7] competing with base pairs from the homologous strand,[8] and permeating the cellular and nuclear membranes.[9] Pyrrole-imidazole (Py-Im) polyamides can recognize nine base pairs of GC, CG, and AT/TA in the DNA minor groove and modulate gene expression with limited anti-tumor efficacy *in vivo*.[10–13] Alternatively, triplex-forming oligonucleotides (TFOs) utilize Hoogsteen (HN) base-pairing rules to recognize the homopurine stretches in the major groove of the duplex DNA.[14] Multiple studies have reported transcription inhibition post TFO-directed triplex formation in the regulatory region of the target genes *in vitro*.[15–18] Overall, low specificity, sequence-restricted recognition, and limited binding affinity pose a significant challenge to the aforementioned DNA binding modalities.

Unlike TFOs, peptide nucleic acid (PNA), a synthetic DNA mimic, can target DNA through WC and HN base-pairing.[19,20] The charge-neutral (2-aminoethyl) glycine backbone imparts enzymatic stability and exhibits higher binding affinity.[21] Prior studies have established that a PNA:DNA heteroduplex has higher thermal stability than a DNA:DNA duplex.[19,22] Several designs, like pseudo-complimentary PNAs,[23] bis-PNAs,[24] and tail-clamp PNAs (tcPNAs),[25] have been explored for genomic DNA invasion. tcPNAs, containing a tail that binds using WC base-pairing and a clamp region that binds with the homopurine region via HN base-pairing, have shown promising results. One study has reported tcPNA-mediated transcription inhibition *in vitro*;[26] however, *in vivo* efficacy and safety have not been demonstrated.

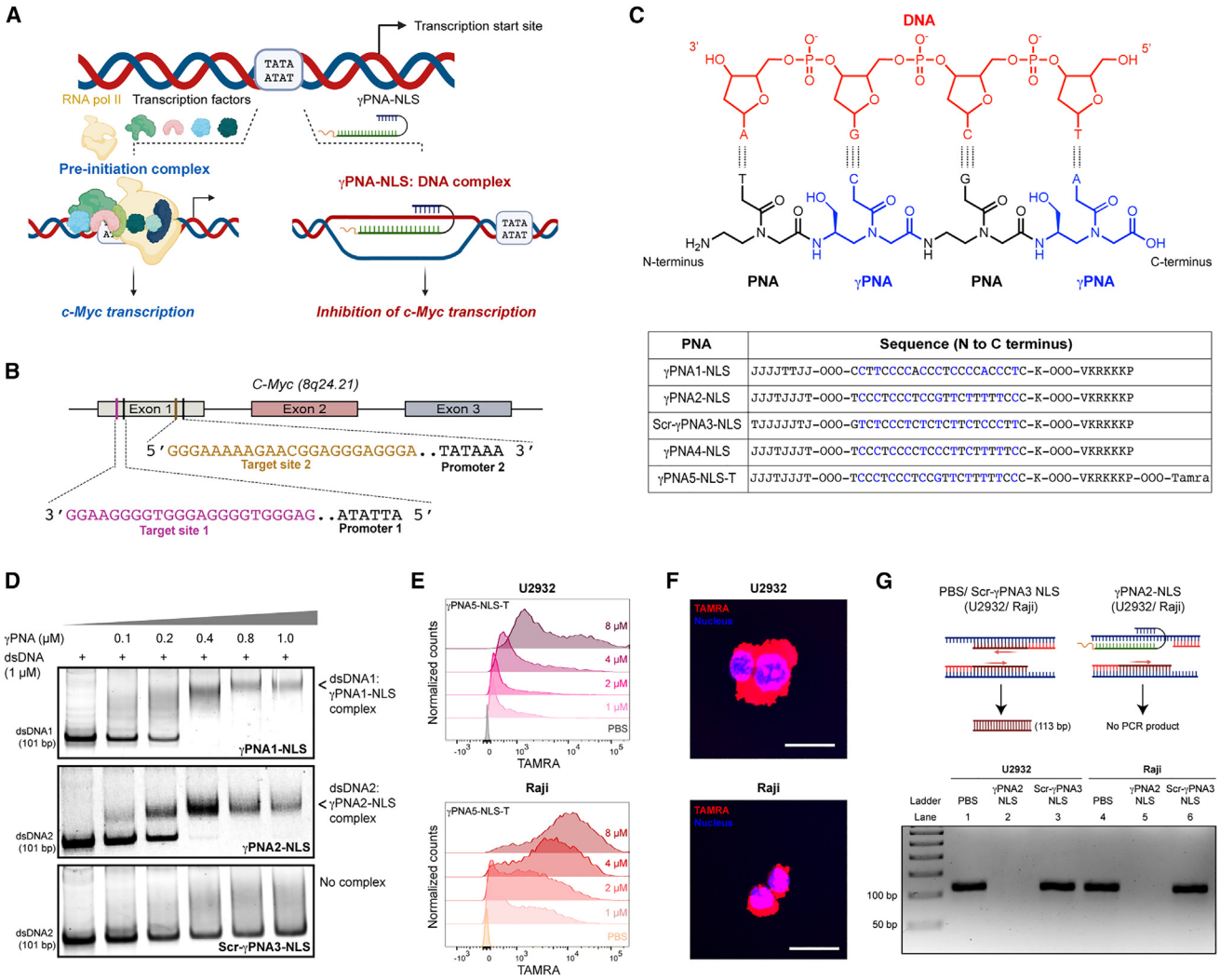

PNA	Sequence (N to C terminus)
γPNA1-NLS	JJJJTTJJ-OOO-CCTTCCCCACCCTCCCCACCCTC-K-OOO-VKRKKKP
γPNA2-NLS	JJJTJJJT-OOO-TCCCTCCCTCCGTTCTTTTTCCC-K-OOO-VKRKKKP
Scr-γPNA3-NLS	TJJJJJTJ-OOO-GTCTCCCTCTCTCTTCTCCCTTC-K-OOO-VKRKKKP
γPNA4-NLS	JJJTJJJT-OOO-TCCCTCCCCTCCCTTCTTTTTCC-K-OOO-VKRKKKP
γPNA5-NLS-T	JJJTJJJT-OOO-TCCCTCCCTCCGTTCTTTTTCCC-K-OOO-VKRKKKP-OOO-Tamra

Figure 1. Design of anti-transcription γPNA-NLS to target the *c-Myc* oncogene

(A) Schematic of γPNA-NLS-mediated inhibition of *c-Myc* transcription.

(B) Graphic representation of target sites in P1 and P2 of the human *c-Myc* oncogene.

(C) Design of gamma peptide nucleic acid (γPNA) conjugated with an NLS to target the indicated sites.

(D) PAGE assay of γPNA1-NLS and γPNA2-NLS at increasing PNA concentrations with dsDNA 1 and 2 containing the respective target site. Scr-γPNA3-NLS was incubated with dsDNA2.

(E) Flow cytometry histograms of lymphoma cells after 24 h treatment with the indicated concentrations of γPNA5-NLS-T.

(F) Confocal microscopy images of live lymphoma cells after 24 h treatment with γPNA5-NLS-T (8 μM). Scale bars, 15 μm.

(G) Amplicon assay confirming binding of γPNA2-NLS (8 μM) to target site 2 in lymphoma cells after 24 h treatment.

To enhance binding affinity and duplex DNA invasion, gamma PNAs (γPNAs) were developed.[27] γPNAs pre-organize into the right-handed helix and can invade the genomic DNA with high binding affinity.[28] While γPNAs have been used for targeted gene editing,[29–31] their potential for targeting genomic DNA in cancer therapy has not been investigated.

Here, we developed an anti-transcription platform targeting the oncogenes at the genomic DNA level. Our approach utilizes the tail-clamp design of γPNAs to invade the critical regulatory regions of the *c-Myc* oncogene to inhibit transcription as a proof of concept (Figure 1A). The *cMyc* oncogene is dysregulated in several cancers.[32] Multiple mechanisms, including gene amplification, chromosomal translocation, activation of enhancers, and alterations in other oncogenic or tumor suppressor proteins, dysregulate the *c-Myc* levels directly or indirectly.[33,34] Direct targeting of c-MYC is difficult because it's a disordered protein that lacks binding pockets and is localized in the nucleus.[35] Several strategies to inhibit *c-Myc* include preventing *c-Myc* translation, decreasing the stability of c-MYC protein, inhibiting the formation of an active heterodimer with Max protein (SaJM589,[36] KI-MS2-008,[37] and KJ-Pyr-9[38]), and inhibiting *c-Myc* transcription.[39] Further, indirect inhibition of bromodomain 4 (BRD4) prevents *c-Myc* transcription and *c-Myc*-mediated transcriptional activation of genes.[40] Peptide-based inhibitors (Omomyc)

sequester MYC in an inactive complex.[41] Small molecules stabilize the G-quadruplexes in *c-Myc*'s promoter region to disrupt its activity.[42] Additionally, an antisense oligonucleotide (INX-3280) was tested in clinical trials but discontinued later.[43,44] Reports also exist on targeting *c-Myc* mRNA utilizing methylphosphonates,[45] small interfering RNAs (siRNAs),[46] and poly-2'-O-(2,4-dinitrophenyl)-RNA[47] with minimal *in vivo* stability.

We conjugated a nuclear localization sequence (NLS) to the γPNA for nuclear delivery. We evaluated the anti-transcription activity of γPNA-NLS in multiple lymphoma cells and animal models, including cell-line-derived xenografts (CDXs), patient-derived xenografts (PDXs), and transgenic mice. Combination therapy has been reported to be effective in cancer treatment as it targets key pathways that act synergistically to induce apoptosis and inhibit angiogenesis, metastasis, and resistance, resulting in robust anti-cancer activity.[48] Histone deacetylase inhibitors (HDACis), clinically approved for the treatment of lymphoma, open the chromatin packing and induce apoptosis of cancer cells via multiple pathways.[49] To increase the accessibility of γPNA-NLS at the target genomic site, we combined the approved HDACi with γPNA-NLS. We noted superior anti-cancer activity in CDX and PDX mouse models compared with γPNA-NLS alone. Similarly, γPNA-NLS-treated xenograft mice showed higher sensitization to doxorubicin, vincristine, cyclophosphamide, and prednisone (CHOP), a first-line therapy for non-Hodgkin's lymphoma (NHL). Hence, corroborated by the inclusive pre-clinical efficacy and safety results, we established γPNA-NLS-mediated genomic DNA targeting as a therapeutic intervention for cancer therapy.

RESULTS

Anti-transcription γPNA design for oncogenic *c-Myc* silencing

The *c-Myc* oncogene, located on chromosome 8 (8 q24.21), contains three exons; exons 2 and 3 encode for the c-MYC protein, while exon 1 spans the critical regulatory elements.[50] Four promoters regulate *c-Myc* transcription. Promoter 1 (P1) and P2, located in exon 1, are the principal promoters driving the transcriptional output of *c-Myc*.[51] In normal cells, P2 regulates 80%–90% of production of steady-state *c-Myc*.[52] However, the translocation of *c-Myc* in Burkitt's lymphoma, t(8; 14)(q24; q32), juxtaposes the *c-Myc* oncogene to the immunoglobulin heavy chain (*IgH*) locus on chromosome 14 and shifts the transcription initiation from P2 to P1 by the enhancers present in the *IgH* locus.[53] We selected target sites upstream of both the major P1 and P2 to design PNAs to inhibit the transcription of the *c-Myc* oncogene (Figure 1B). Target site 1 is 100 bp upstream of P1 on the template strand and is required for binding of nuclear factors to initiate transcription.[52] Target site 2 is 10 bp upstream of P2 on the coding strand and has been established to be the binding site for multiple transcription factors, including the E2 factor (E2F) and E26 transformation-specific (ETS) family[54] and MYC-associated zinc-finger (MAZ) protein.[55] MAZ recognizes a specific GA (GGGAGGG) region in target site 2 to regulate *c-Myc* transcription.[55] Prior studies have reported that targeting the selected sites in exon 1 inhibits *c-Myc* transcription *in vitro*.[15]

Here, we designed anti-transcription tail clamp γPNA constructs complementary to the selected *c-Myc* target sites. To achieve selectivity, we targeted 23-mer target regions containing homopurine stretches that allow the PNAs to form a clamp via HN base-pairing. A series of tail-clamp γPNAs was synthesized using Boc chemistry-based solid-phase synthesis protocols[56] (Figure 1C). The serine-γPNA monomers were introduced at alternate positions in the WC binding domain of γPNAs. Prior work established that partial γ substitution is sufficient to confer helical pre-organization.[29,31] A classical nuclear localization signal (PKKKRKV) was conjugated to the C terminus (3′ end) of PNAs to improve nuclear delivery.[57] γPNA1-NLS binds to the target site upstream of P1 on the template strand, and γPNA2-NLS is complementary to the purine-rich region upstream of P2 on the coding strand. A scramble sequence, Scr-γPNA3-NLS, was used as a control. γPNA4-NLS was designed to bind upstream of P2 in the mouse *c-Myc* oncogene (mouse *Myc* target sequence: 5′-GGAAAAAGAAGGGAGGGGAGGGA-3′), which differs from the human *Myc* sequence. γPNA5-NLS-T had the same sequence as γPNA2-NLS and contained a 5-carboxytetramethylrhodamine (TAMRA) fluorophore for visualization. Reverse-phase high-performance liquid chromatography (RP-HPLC) was used to purify the synthesized γPNAs (Figures S1A–S1D), and molecular weight was determined by mass spectrometry (Table S1). An electrophoretic mobility assay confirmed the formation of a stable invasion complex post incubation of γPNA1-NLS and γPNA2-NLS constructs with the double-stranded DNA (dsDNA) 1 and 2 (101 bp) containing their respective target sites. We noted complete binding of the γPNA1-NLS and γPNA2-NLS with their targets at a low dsDNA:PNA (1:0.4) molar ratio. As expected, Scr-γPNA3-NLS showed no binding (Figure 1D). Our recent study described that adding cationic amino acids to PNAs increases the binding affinity toward the target RNA site.[58]

Anti-transcription γPNA-NLS undergoes internalization and invades the genomic DNA

We assessed the uptake of γPNA-NLS *in vitro* to ensure cytoplasmic and nuclear localization. We used two lymphoma cell lines, including U2932, a diffuse large B cell lymphoma (DLBCL), and Raji, a Burkitt's lymphoma, whose proliferation is driven by the *c-Myc* oncogene.[59] γPNA5-NLS-T showed a dose-dependent increase in internalization in U2932 and Raji cells based on flow cytometry analysis (Figure 1E). We noted considerable uptake of γPNA5-NLS-T at 8 μM after 24 h of incubation. Corroborated by confocal microscopy, treated U2932 and Raji cells showed a significant accumulation of γPNA5-NLS-T in the cytoplasm and nucleus (Figure 1F). We observed similar results in cervical carcinoma (HeLa) cells, where *c-Myc* amplification is associated with poor survival (Figure S1E).[39] The 3-dimensional volume plot of treated HeLa cells confirmed the accumulation of γPNA5-NLS-T inside the nucleus (Figure S1F). Next, we used an PCR amplicon assay to ensure the invasion of γPNA2-NLS at the target genomic site in treated U2932 and Raji cells. The binding of γPNA2-NLS at the target site will sterically hinder the DNA polymerase-mediated extension of the flanking primers to form the amplicon. We isolated the DNA from control (PBS) and γPNA2-NLS- and Scr-γPNA3-NLS-treated lymphoma cells and amplified

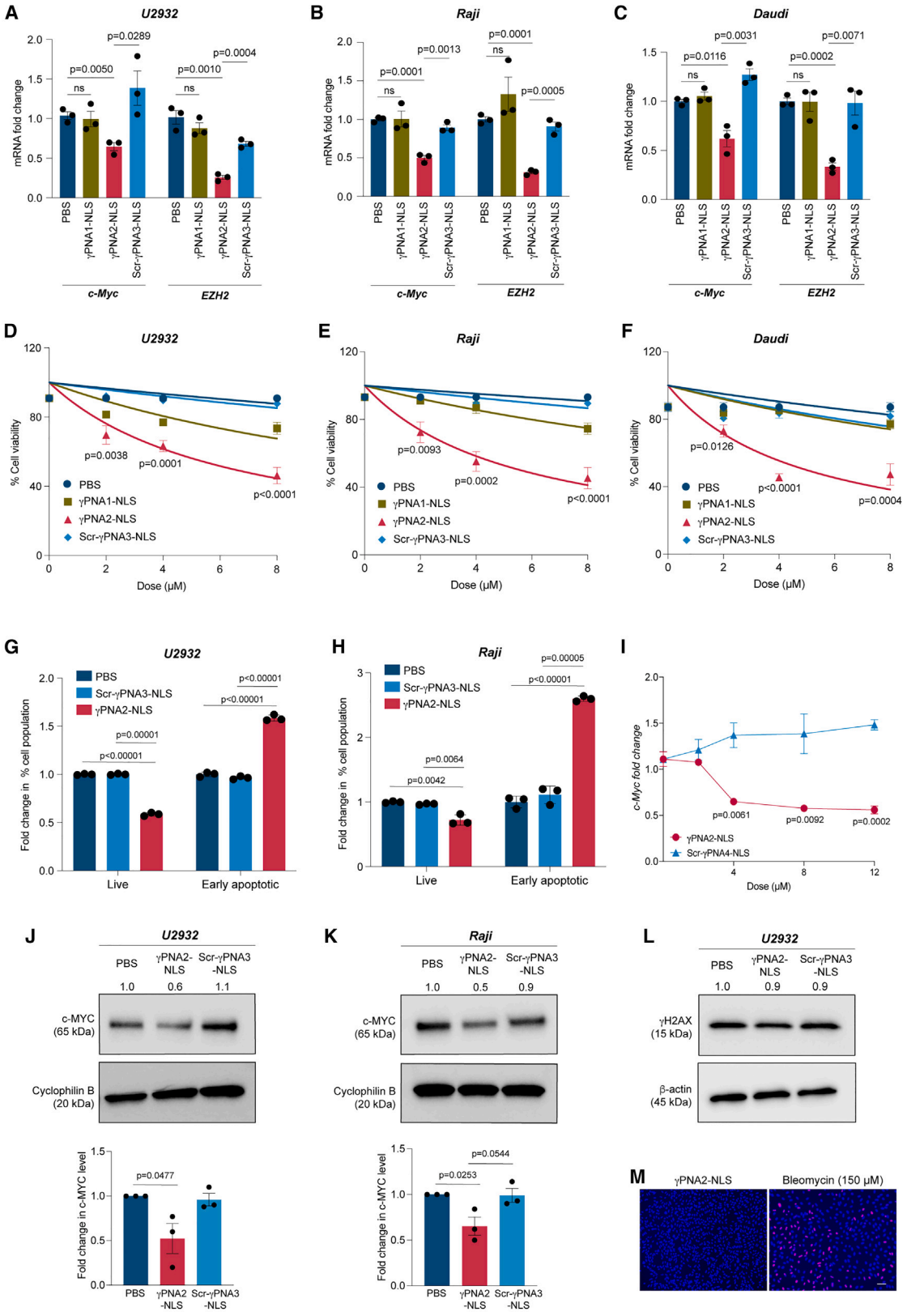

(legend on next page)

the target region upstream of P2 in the *c-Myc* locus. As expected, control and Scr-γPNA3-NLS-treated cells showed 113-bp amplicons post separation on an agarose gel (Figure 1G). The treatment of U2932 cells with γPNA2-NLS resulted in a dose-dependent decrease in the amplicon intensity (Figure S1G), while no product was observed in either U2932 or Raji cells at 8 μM (Figure 1G). These results confirmed the selective binding of γPNA at the target genomic DNA location.

Transcriptional silencing of *c-Myc* in lymphoma cells

We evaluated the activity of γPNA-NLS constructs in U2932 and Burkitt's lymphoma (BL) cell lines (Raji and Daudi). Exon 1, containing the regulatory elements of *c-Myc* transcription, is intact in both BL cell lines and was selected for evaluating the efficacy of designed γPNA-NLS targeting the major promoters (P1 and P2) of the *c-Myc* oncogene.[53] We quantified the gene expression levels of *c-Myc* and its downstream target enhancer of zeste homolog 2 (*EZH2*) in the cells after treatment with γPNA-NLS. *EZH2* overexpression arrests B lymphocytes in an immature state and causes repression of tumor suppressors, leading to perpetual proliferation of B cells.[60] Small-molecule inhibitors of EZH2 protein are being used for the treatment of refractory follicular lymphomas, and others are being tested in various stages of clinical trials to treat solid tumors and diffuse large B cell lymphomas.[61] *EZH2* is a *bona fide* oncogene, and *c-Myc* upregulates *EZH2* via repression of miR-26a.[62] We observed 35% and 75% downregulation of *c-Myc* and *EZH2* in U2932 cells treated with γPNA2-NLS (Figure 2A). γPNA1-NLS did not affect the gene expression levels of *c-Myc* or *EZH2*. This was expected because U2932 cells contain wild-type *c-Myc*, where P2 is the primary regulator of *c-Myc* transcription. Similarly, γPNA2-NLS treatment resulted in 50% and 38% downregulation of *c-Myc* (Figures 2B and 2C) in Raji and Daudi cells, respectively. *EZH2* levels were reduced by 69% in Raji and 66% in Daudi cells after treatment with γPNA2-NLS. Due to the chromosome translocation of *c-Myc* in Raji and Daudi cells, P1 also contributes to *c-Myc* transcription.[63] However, γPNA1-NLS did not induce *c-Myc* downregulation. This raises the possibility that the target site upstream of P1 is inaccessible to γPNA1-NLS. In addition, targeting P2 in Raji and Daudi cells can decrease *c-Myc* transcription by inhibiting the transcription from P2 and interfering with the progression of the transcript initiated from P1. To ensure the efficacy of γPNA2-NLS in the other cell lines, we assessed *c-Myc* expression in the HeLa, hepatocellular carcinoma (HepG2), lung adenocarcinoma (A549), triple-negative breast cancer (MDA-MB-231), and prostate cancer (PC3) cells post treatment. γPNA2-NLS treatment resulted in 56% and 50% knockdown of *c-Myc* in HeLa and HepG2 cells, respectively (Figures S1H and S1I), while γPNA1-NLS showed only a 22% decrease of *c-Myc* in both cell types relative to the PBS-treated group. Similarly, we observed that γPNA2-NLS resulted in a 62% decrease in *c-Myc* levels in A549 cells post treatment (Figure S1J). Scr-γPNA3-NLS had no effect on *c-Myc* expression in the tested cell lines. γPNA2-NLS treatment resulted in 31% and 45% knockdown of *c-Myc* in MDA-MB-231 and PC3 cells, respectively (Figure S1K).

γPNA2-NLS binds to the coding strand at the target genomic location. To rule out that it can bind to the mRNA initiated from P1, we designed an antisense oligonucleotide (ASO) with the same sequence as γPNA2-NLS. The anti-cMyc ASO can target the *c-Myc* mRNA and induce its degradation by activating RNase H1. We did not notice a decrease in *c-Myc* levels in U2932 and Raji cells transfected with ASO using RT-PCR analysis (Figure S1L). Similarly, no reduction of c-MYC protein was observed in U2932 or Raji cells treated with the ASO (Figure S1M). We confirmed that γPNA2-NLS-mediated inhibition of *c-Myc* is due to its anti-transcription activity.

Next, we assessed the viability of lymphoma cells treated with PBS, γPNA1-NLS, γPNA2-NLS, and Scr-γPNA3-NLS at different doses using a trypan blue assay. γPNA2-NLS treatment showed a greater than 50% reduction in the viability of U2932, Raji, Daudi, MDA-MB-231, and PC3 cells (Figures 2D–2F and S1N). Annexin V staining of γPNA2-NLS-treated U2932 (Figure 2G) and Raji cells (Figure 2H) resulted in an ∼1.5- and 2.5-fold increase in early apoptotic cells, respectively. We tested the efficacy of γPNA2-NLS at higher doses in both U2932 and Raji cells. We did not observe a decrease in the levels of *c-Myc* beyond 50%, even at the 12 μM dose (Figures 2I and S1O). This can be due to various factors, including saturation of endocytic receptors, endosomal entrapment, limited nuclear accumulation, or moderate accessibility to the target sites due to other transcription factors.

We performed western blot (WB) analysis to determine the change in c-MYC and EZH2 proteins. We noted an ∼50% reduction of c-MYC in γPNA2-NLS-treated U2932 (Figure 2J) and Raji cells (Figure 2K) relative to control and Scr-γPNA3-NLS treatment. Similarly, γPNA2-NLS treatment resulted in 20%–40% lower EZH2 levels in U2932 (Figure S1P) and Raji cells (Figure S1Q).

To investigate whether γPNA2-NLS-mediated strand invasion in the P2 region of the *c-Myc* locus induced DNA damage, we determined the change in phosphorylated histone H2A protein (γH2AX), a marker of double-strand breaks (DSBs), via WB, immunofluorescence analyses, flow cytometry, and comet assay.

Figure 2. Anti-transcription activity of γPNA-NLS in lymphoma cells

(A–C) Relative fold change in *c-Myc* and *EZH2* after treatment with PBS and the indicated γPNAs (8 μM) for 24 h.

(D–F) Percentage of viability of lymphoma cells treated with PBS, γPNA1-NLS, γPNA2-NLS, and Scr-γPNA3-NLS for 24 h.

(G and H) Fold change in live and early apoptotic lymphoma cells after 24 h treatment with γPNA2-NLS and Scr-γPNA3-NLS (8 μM).

(I) Relative change in *c-Myc* in U2932 cells treated with the indicated γPNA2-NLS doses in comparison with Scr-γPNA3-NLS.

(J and K) Representative WBs of c-MYC protein in lymphoma cells (top) after 24 h treatment with PBS (control), γPNA2-NLS, and Scr-γPNA3-NLS (8 μM). Graphs represent the quantification of c-MYC protein fold change relative to PBS.

(A–K) Graphs show mean ± SEM (n = 3); p value for unpaired two-sample t test.

(L) WB representing levels of γH2AX protein in γPNA2-NLS and Scr-γPNA3-NLS (8 μM) after 24 h relative to PBS.

(M) Representative immunofluorescence images of HeLa cells stained with γH2AX antibody after 24 h treatment with γPNA2-NLS (8 μM) and bleomycin. Scale bar, 50 μm.

U2932 cells treated with γPNA2-NLS and Scr-γPNA3-NLS did not induce an increase in γH2AX protein (Figure 2L). Immunofluorescence staining of γH2AX in γPNA2-NLS-treated HeLa cells showed no signs of DNA damage, while bleomycin-treated cells showed increased γH2AX-positive nuclei (Figures 2M, S1R, and S1S). Flow cytometry corroborated these results, where no difference in γH2AX-positive U2932 cells was observed (Figure S1T). A neutral comet assay, used to measure the DSBs, showed no difference in the percentage of DNA tail region in U2932 cells treated with γPNA2-NLS or PBS (Figure S1U). These results confirmed that the designed γPNA2-NLS does not exert genotoxicity. To confirm chromosomal binding, we treated MDA-MB-231 cells with γPNA5-NLS-T. We arrested the cells in metaphase and observed 2–4 red foci per cell in the nucleus, indicating γPNA5-NLS-T binding to its target site (Figure S1V).

Transcriptome sequencing revealed impairment of DNA replication and repair pathways after silencing of *c-Myc*

c-Myc regulates the transcription of genes associated with cellular proliferation, protein synthesis, DNA replication, and metabolism, which drive the aggressive clinical behavior of lymphomas.[40] We performed RNA sequencing to assess the transcriptomic profile of U2932 lymphoma cells after γPNA2-NLS-mediated transcription inhibition of *c-Myc* for 72 h. We found 913 differentially expressed genes (DEGs) in γPNA2-NLS-treated U2932 cells. We noted that most DEGs obtained from sequencing analysis showed protein-protein interaction (PPI) when analyzed using the search tool for the retrieval of interacting genes/protein (STRING) database (Figure S2A).[64] Functional enrichment of these genes highlighted multiple biological processes, including the cellular metabolic process, cellular localization, biosynthetic process, and nucleic acid metabolic process, that were affected after *c-Myc* inhibition. Network analysis of the DEGs enriched in the nucleic acid metabolic process showed alteration in nucleotide metabolism in U2932 cells after inhibition of *c-Myc* transcription (Figure S2B). We performed Gene Ontology (GO) analysis of DEGs to identify the pathways after inhibition of *c-Myc* transcription. We noted enrichment of downregulated DEGs in RNA splicing, DNA replication, and repair pathways (Figure 3A). We observed that the upregulated DEGs were enriched in RNA catabolic processes, pathways, and proteins targeting the membrane or endoplasmic reticulum (Figure S2C).

The PPI analysis of downregulated DEGs enriched in RNA splicing (Figure S2D), DNA replication (Figure S2E), and dsDNA repair (Figure S2F), using the STRING database, highlighted several genes involved in the replication of cancer cells. For validation, we selected the breast cancer type 2 susceptibility protein (*BRCA2*), which prevents degradation of stalled replication forks;[65] radiation sensitive 52 (*Rad52*) and X-ray repair cross-complementing (*XRCC2*) with a role in homologous recombination;[66] DNA ligase 4 (*LIG4*)[67] and petite integration frequency 1 (*PIF1*)[68] with DNA helicase activity; and claspin (*CLSPN*)[69] and Fanconi anemia complementation group M (*FANCM*),[70] essential for DNA replication and DNA damage response (DDR). Oncogene-induced replication stress (RS) relies on the DDR pathways to ensure the progression of stalled replication forks.[71] In the absence of DDR activation, RS reduces the proliferation and induces apoptosis of cancer cells. Hence, selective targeting of DDR components is being explored extensively as a therapeutic approach to sensitize resistant tumors against available anti-cancer therapies.[72] From the RNA splicing pathway, we selected CDC2-like protein kinases (*CLK*), including *CLK1*, *CLK2*, *CLK4*, and serine/arginine-rich splicing factor 10 (*SRSF10*), with an established role in alternative splicing and tumorigenesis.[73] We selected downregulated DEGs associated with transcription (*E2F3* [E2F transcription factor 3] and *BRD9* [bromodomain 9]),[74,75] translation (*EIF5B* [eukaryotic translation initiation factor 5B] and *EIF4EBP3* [eukaryotic translation initiation factor 4E binding protein 3]), and metabolism (*OGT* [O-liked N-acetylglucosaminyltransferase])[76] with a potential role in maintaining the proliferation of cancer cells.

The expression levels of the selected genes were validated in U2932 cells treated with PBS, γPNA2-NLS, and Scr-γPNA3-NLS using RT-PCR. We confirmed 60% downregulation of *c-Myc* in the γPNA2-NLS-treated group (Figure S2G). Consistent with the RNA sequencing (RNA-seq) results, we observed a 2-fold increase in ADP ribosylation factor-like GTPase 11 (*ARL11*), a tumor suppressor gene,[77] in γPNA2-NLS-treated U2932 cells (Figure S2H). We noted downregulation of the selected genes (Figures 3B, S2I, and S2J) in U2932 cells.

Next, we performed RNA-seq in U2932 cells using an siRNA-positive control and compared it with γPNA2-NLS-treated cells after 48 h. siRNA targeting *c-Myc* showed a 55% decrease in *c-Myc* levels and was comparable with γPNA2-NLS (45%) in U2932 cells (Figure S2K). Hierarchical cluster analysis of DEGs was used to assess genes impacted by *c-Myc* inhibition in both treatment groups. We observed a number of the upregulated (66) and downregulated (37) common DEGs between the γPNA2-NLS- and siRNA-treated groups (Figure 3C). We performed gene set enrichment analysis (GSEA), and *c-Myc* gene sets were downloaded from the GSEA website. Enrichment was considered significant when nominal $p < 0.05$. A positive normalized enrichment score (NES) indicates that genes expressed in the γPNA2-NLS and siRNA groups are enriched in the respective *c-Myc* GSEA dataset compared with the control. Three datasets showed significant gene overlap and were common between both groups (Figure 3D).

We identified the potential off-target sites of γPNA2-NLS using BLAST analysis against the NCBI transcript reference sequences (taxid: 9606). Intersection of the potential off-target genes with the DEGs (368) obtained from RNA-seq analysis showed no overlap. These results suggest minimal off-target activity of γPNA2-NLS (Figures S2L and S2M).

In vivo efficacy of anti-transcription γPNA-NLS in the U2932 xenograft mouse model

We evaluated the biodistribution of γPNA-NLS in a subcutaneous U2932 CDX mouse model. We performed systemic administration of γPNA5-NLS-T in U2932 xenograft mice and performed *in vivo* imaging using the *in vivo* imaging systems (IVIS) at different time points. γPNA5-NLS-T accumulated in the tumors starting at 0.25 h and showed moderate retention until 24 h (Figures 4A and S3A). IVIS imaging of the tumors and major organs isolated from treated mice at 6 h and 24 h showed strong fluorescence in the tumor relative to control mice (Figure 4B). We analyzed the log-transformed fluorescence signal using exponential one-phase decay and determined an *in vivo* half-life of PNA as 2.3 h.

CellPress
OPEN ACCESS

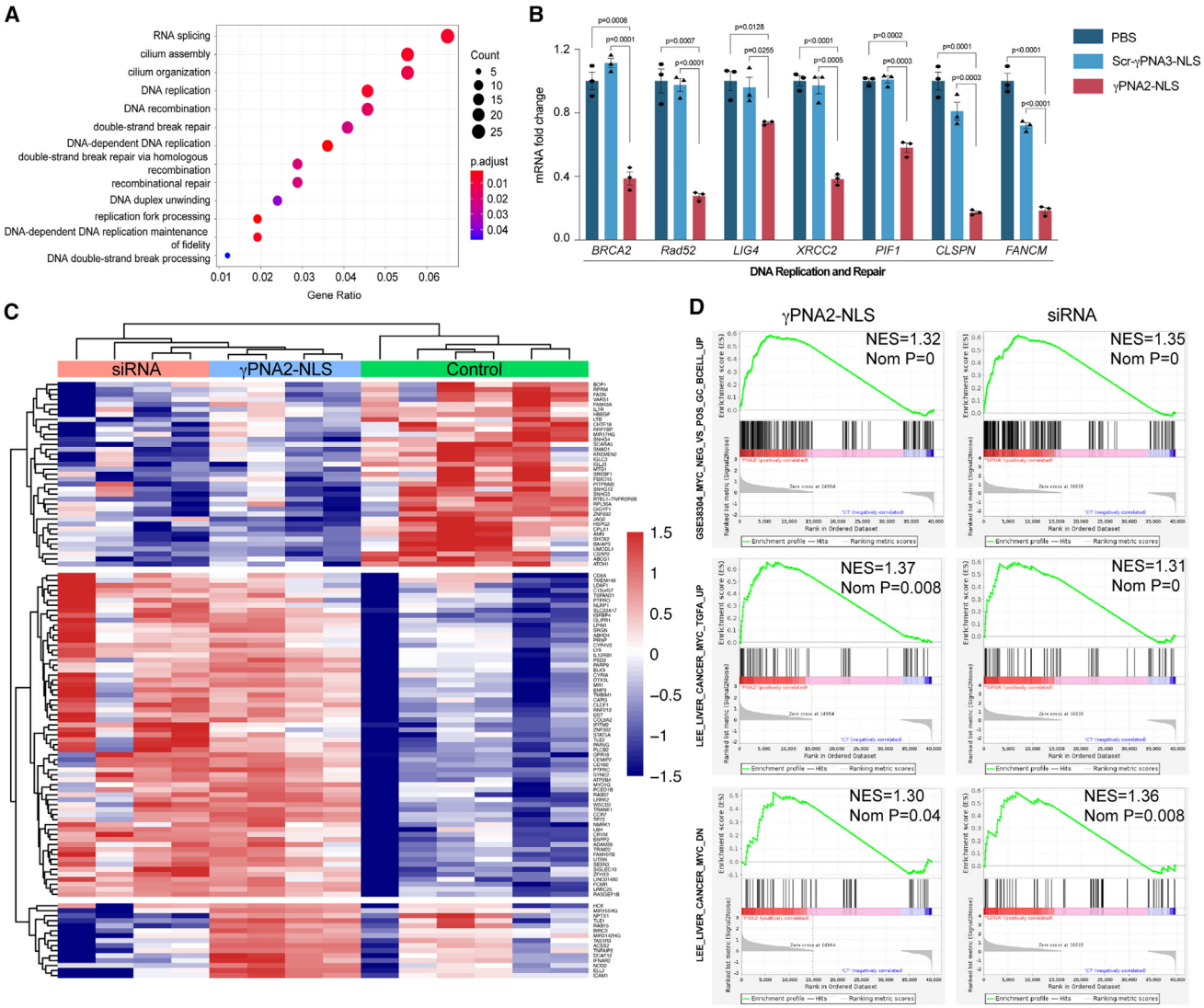

Figure 3. Transcriptome sequencing analysis after *c-Myc* silencing

(A) GO analysis of downregulated DEGs.

(B) RT-PCR-based validation of the downregulated DEGs associated with DNA replication and repair in U2932 cells treated with PBS (control), γPNA2-NLS, and Scr-γPNA3-NLS (8 μM) for 72 h. Graphs show mean ± SEM (n = 3); p value for unpaired two-sample t test.

(C) Hierarchical clustering analysis of DEGs after treatment of U2932 cells with γPNA2-NLS and siRNA compared with PBS treatment.

(D) Enrichment plots for the top three datasets enriched in GSEA, showing NES and normalized p value.

We observed fluorescence in the kidneys, which is expected as it is the primary site for PNA elimination. Confocal microscopy confirmed the substantial accumulation of γPNA5-NLS-T within the tumors at 6 h and 24 h (Figure 4C).

To determine the efficacy of γPNA2-NLS *in vivo*, we tested its activity in two cell-line-derived (U2932 and Raji cells) xenograft mouse models (Figures S3B and S3C). In U2932-derived xenograft mice, γPNA2-NLS was injected intravenously (i.v.) at a single dose of 25 mg/kg, followed by evaluation of c-MYC knockdown via WB analysis after 24 h. We observed a 50% decrease in c-MYC (Figures 4D and 4E) and a 10% decrease in EZH2 protein (Figures 4D and S3D) in γPNA2-NLS-treated mice. Next, we tested the efficacy of γPNA2-NLS in Raji cell-derived xenografts after intra-tumoral (i.t.) administration at a lower dose of 5 mg/kg. WB analysis showed a 40% decrease in c-MYC protein in γPNA2-NLS-treated Raji cell tumors and a moderate reduction in EZH2 levels (Figures 4F and 4G).

We studied the efficacy of γPNA2-NLS in U2932 and MDA-MB-231 CDX mice. Xenograft tumors of about 100–150 mm^3 were treated systemically with four doses of γPNA at 5 mg/kg over 10 days (Figure S3E). γPNA2-NLS-treated mice showed a 2-fold reduction (day 10) in the tumor volumes compared with saline- or Scr-γPNA3-NLS-treated mice (Figure 4H). The survival endpoint was when tumors reached 2,000 mm^3. Mice treated with γPNA2-NLS had a median survival of 27 days, while the saline and Scr-γPNA3-NLS group survived until 21 days (Figure S3E).

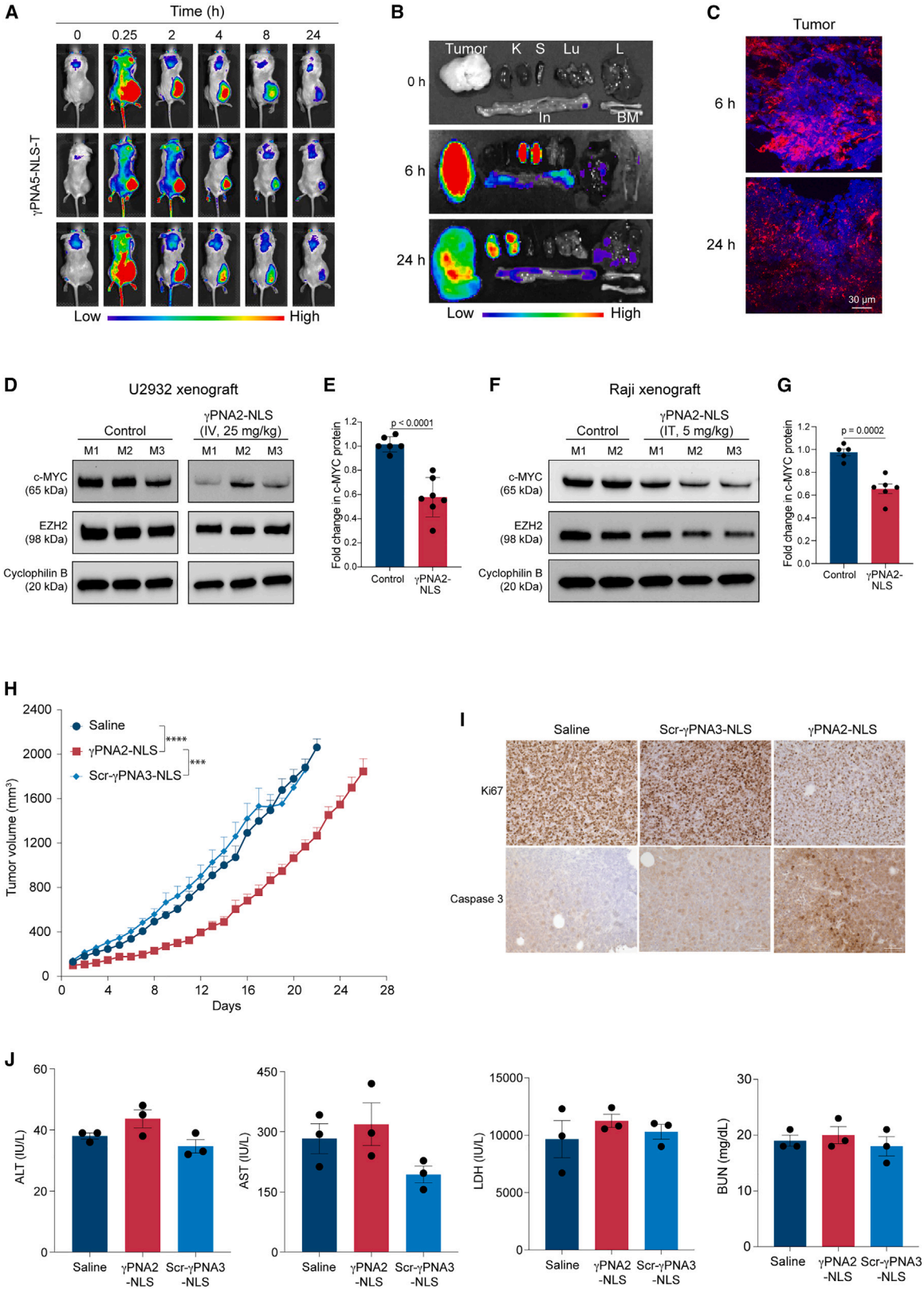

(legend on next page)

These results were corroborated by the downregulation of c-MYC (~55%) and EZH2 (~20%) levels in γPNA2-NLS-treated tumors (Figures S3F and S3G). We performed histological (Figure S3H) and immunohistochemical analyses, including Ki67, a proliferation marker, and caspase 3, an apoptotic marker (Figure 4I), in tumors post survival study. We noted reduced staining of Ki67 and an increase in caspase-3 in γPNA2-NLS-treated tumors (Figure S3I). These results confirmed the efficacy of γPNA2-NLS to inhibit *c-Myc* transcription and arrest tumor growth. In MDA-MB-231 CDX mice, γPNA2-NLS-treated mice showed a 2-fold reduction (days 15–25) in tumor volumes compared with control mice (Figure S3J).

To ensure the safety of designed γPNA constructs, we evaluated the complete blood count (CBC), blood chemistry, and histopathological analysis of organs in all treatment groups of U2932 xenografts. We did not notice a change in mouse weight during the tumor growth study in the treatment groups relative to the saline (Figure S3K). No change in liver enzymes (alanine transaminase, aspartate transaminase, lactate dehydrogenase) or blood urea nitrogen (BUN) was observed in the treated mice (Figure 4J). Likewise, CBC parameters showed no signs of toxicity (Figure S3L). Histological analysis of major organs did not show any morphological changes in the tissues (Figure S3M). Overall, these results confirmed the safety of γPNA-NLS *in vivo*.

Efficacy of anti-transcription γPNA2-NLS with HDACis and chemotherapeutic drugs

Chromatin packing by nucleosomes hinders genome access for transcription and replication machinery.[78] The dynamic protein-DNA complex is regulated by histone acetylation and methylation. Balancing HDAC and histone acetyltransferase (HAT) activity controls chromatin condensation and gene expression.[79] Cancer cells overexpress HDACs, making them sensitive to HDACis, which prevent tumor growth.[80] Several HDACis have been approved for cancer treatment, with better results when combined with other anti-cancer drugs, particularly for resistant cancers.[49] To improve the anti-transcription γPNA2-NLS efficacy, we considered sensitizing the cancer cells by pre-treating them with HDACis. We hypothesized that HDACi-mediated chromatin relaxation would enhance the accessibility of γPNA2-NLS at the target site. We tested the activity of γPNA2-NLS in lymphoma cells pre-treated with Food and Drug Administration (FDA)-approved HDACis, including romidepsin and vorinostat.[81] γPNA2-NLS showed higher activity in U2932 cells pre-treated with romidepsin. It resulted in a 66% and 79% reduction in viability on days 2 and 4, respectively, relative to the cells treated with only romidepsin or γPNA2-NLS (50% viability, day 4) (Figure 5A). We observed similar results in U2932 cells treated with γPNA2-NLS and vorinostat, which showed 78% reduced viability on day 4 (Figure S4A). As expected, Scr-γPNA3-NLS did not show synergistic activity when tested with romidepsin or vorinostat in U2932 cells. RT-PCR-based quantification confirmed our hypothesis that pre-treatment of U2932 cells with romidepsin resulted in 5- and 1.4-fold lower *c-Myc* and *EZH2* levels, respectively (Figure 5B). Vorinostat combined with γPNA2-NLS resulted in an ~6-fold reduction in *c-Myc* and an ~7-fold decrease in *EZH2* levels (Figure S4B). We tested the activity of γPNA2-NLS with valproic acid, which reduces chromatin condensation and promotes demethylation of DNA.[82] We observed 78% lower viability in γPNA2-NLS- and valproic acid-treated U2932 cells and a 3-fold decrease in *c-Myc* levels compared with only valproic acid treatment (Figures S4C and S4D). WB analysis of lysates from U2932 cells treated with the combination of romidepsin and γPNA2-NLS resulted in 6- and 1.5-fold lower c-MYC and EZH2 protein relative to romidepsin (Figure 5C). We confirmed our results by testing γPNA2-NLS and romidepsin in Raji cells using viability and gene expression analyses. The combination treatment resulted in 75% lower viability, while only romidepsin-treated cells showed a 58% reduction in viability of Raji cells on day 4 (Figure S4E). We noted 3.3-fold lower *c-Myc* levels in Raji cells treated with γPNA2-NLS and romidepsin (Figure S4F). In addition, 24 h pre-treatment with romidepsin followed by 24 h treatment with γPNA2-NLS showed superior knockdown of *c-Myc* and *EZH2* in both U2932 (Figure S4G) and Raji cells (Figure 5D) in comparison with romidepsin treatment. The increased activity of γPNA2-NLS, when combined with multiple HDACis in lymphoma cells, established the potential of γPNA2-NLS as a combination therapy for the treatment of resistant cancers.

After γPNA2-NLS mediated *c-Myc* transcription inhibition, RNA sequencing showed significant downregulation of genes associated with DNA replication and repair pathways, indicating sensitization of lymphoma cells to chemotherapeutic drugs. Pre-treatment of U2932 cells with γPNA2-NLS (24 h) followed by CHOP treatment resulted in 2-fold lower viability compared with CHOP-only-treated cells (Figure 5E). These results confirmed that γPNA2-NLS enhances the efficacy of approved anti-cancer drugs.

In vivo efficacy of γPNA2-NLS and romidepsin in U2932 xenograft mice

We investigated the anti-tumor activity of γPNA2-NLS with romidepsin in U2932 xenograft mice. To sensitize the mice, romidepsin was administered intraperitoneally 24 h before the first and

Figure 4. Efficacy of anti-transcription γPNA-NLS in lymphoma xenograft mice

(A) IVIS images of U2932 xenografts post γPNA5-NLS-T administration at the indicated time points (5 mg/kg dose, i.v.).

(B) IVIS images of tumor and organs, including kidneys (K), lungs (Lu), liver (L), spleen (S), intestine (In), and bone marrow (BM), after γPNA5-NLS-T administration.

(C) Confocal images of γPNA5-NLS-T treated xenografts. Blue, DAPI.

(D and E) c-MYC and EZH2 protein levels (D) and quantification (E) in control and γPNA2-NLS-treated (25 mg/kg, i.v.) U2932 xenografts after 24 h (control, n = 6; γPNA2-NLS, n = 7).

(F and G) c-MYC and EZH2 protein levels (F) and quantification (G) in control and γPNA2-NLS-treated (5 mg/kg, i.t.) Raji xenografts after 24 h (control, n = 5; γPNA2-NLS, n = 6).

(E and G) Graphs show mean ± SEM; p value for unpaired two-sample t test.

(H) Tumor growth curve of U2932 xenograft mice treated with γPNA2-NLS and Scr-γPNA3-NLS (5 mg/kg) (saline, n = 10; γPNA2-NLS, n = 9; Scr-γPNA3-NLS, n = 8). Mean ± SEM; p value for two-way ANOVA.

(I) Immunohistochemistry of tumors, including Ki67 and caspase-3, staining in U2932 xenografts post survival study. Scale bar, 50 μm.

(J) Serum chemistry analysis of U2932 xenografts post survival. Graphs show mean ± SEM (n = 3).

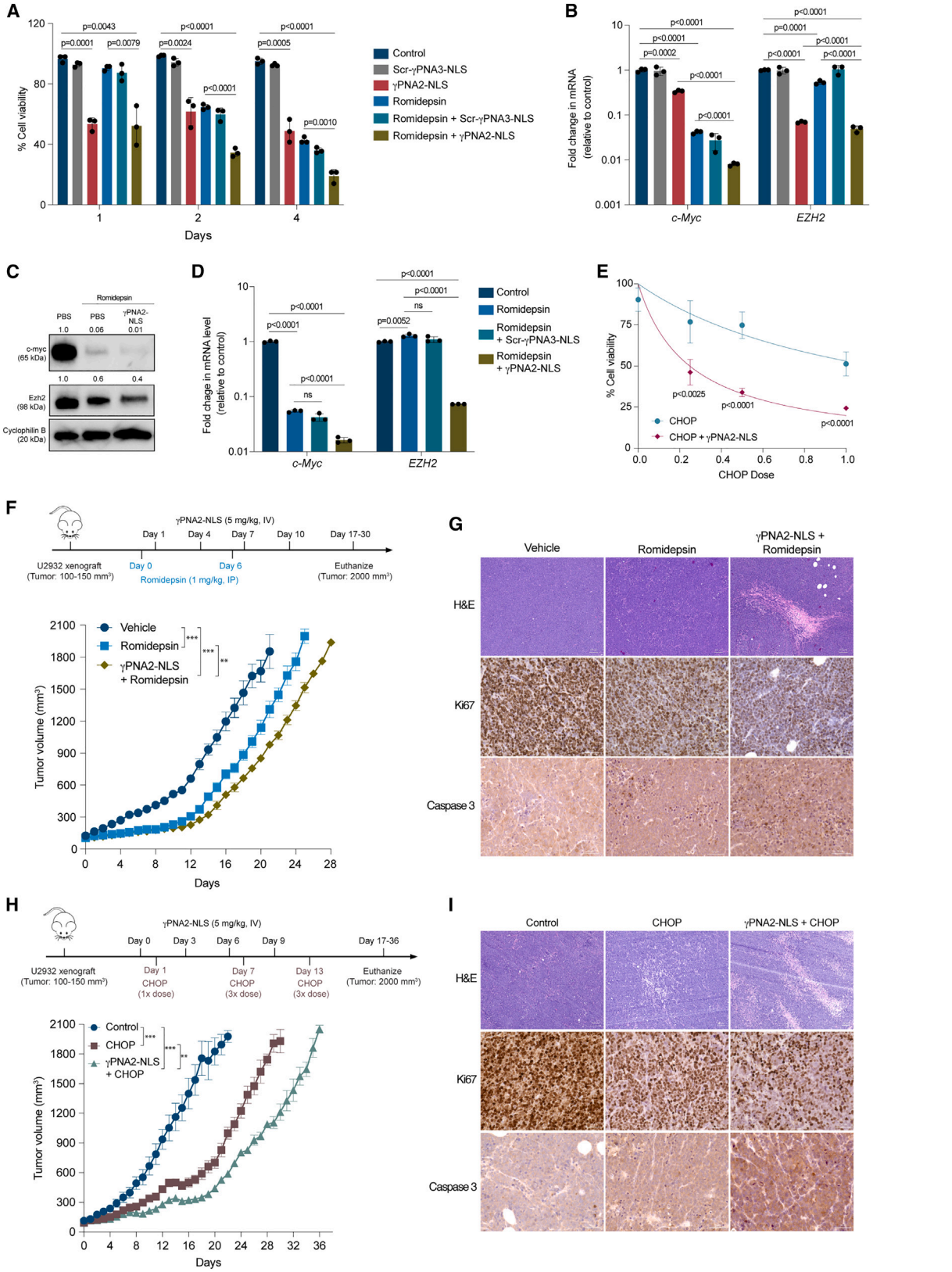

(legend on next page)

third doses of γPNA2-NLS (Figure 5F). U2932 tumors treated with romidepsin reduced the tumor growth by 2-fold. The combination of γPNA2-NLS and romidepsin showed a 3-fold decrease in tumor volume relative to the vehicle on day 12 (Figures 5F, S4H, and S4I). We noted a median survival of 29 days in mice treated with γPNA2-NLS and romidepsin, while romidepsin-only-treated mice survived until 25 days (Figure S4J). H&E staining of tumors indicated tissue disruption in the γPNA2-NLS- and romidepsin-treated group in addition to the reduction in Ki67-positive cells and higher caspase-3 activations relative to the romidepsin- or vehicle-treated group (Figures 5G, S4K, and S4L). We did not notice a change in the weight of mice from different groups (Figure S4M). CBC and histological analysis of organs established the safety of the combination therapy *in vivo* (Figures S4N and S4O). These results confirmed that improving the accessibility of γPNA2-NLS at the target site using HDACis is an effective approach.

In vivo efficacy of γPNA2-NLS with CHOP in U2932 xenograft mice

We evaluated the efficacy of γPNA2-NLS as a combination therapy with CHOP in the U2932 xenograft mouse model. To minimize the toxicity associated with the CHOP regimen, we administered three incremental doses of CHOP over 13 days and four doses of γPNA2-NLS (Figure 5H). We observed 3.2- and 2-fold lower tumor volumes on day 10 (Figure S5A) in γPNA2-NLS plus CHOP and CHOP-treated mice, respectively (Figures 5H and S5B). Mice treated with the combination of γPNA2-NLS and CHOP showed a median survival of 34 days versus 29 days after CHOP treatment (Figure S5C). Histological analysis revealed disrupted tissue in γPNA2-NLS- and CHOP-treated mice (Figure 5I). Similarly, immunohistochemical staining of tumor sections showed a minimum of proliferative cells, as indicated by reduced Ki67 staining, and maximum caspase-3 activation in γPNA2-NLS- plus CHOP-treated mice compared with the CHOP treatment (Figures 5I, S5D, and S5E). We did not observe more than a 10% decrease in 'mouse weight post treatment with CHOP or γPNA2-NLS plus CHOP relative to the control mice (Figure S5F). We noted a marginal reduction in red blood cells, hemoglobin, and platelets in CHOP-treated mice (Figure S5G). H&E staining confirmed no change in the organ histology except for the spleen, which showed splenomegaly in CHOP-treated mice (Figure S5H). This observation is consistent with the reports of cytotoxic drug-mediated toxicity in mice.[83] These findings establish the potential of anti-transcription γPNA2-NLS to improve the therapeutic index of cytotoxic drugs.

The anti-transcription activity of γPNA-NLS in transgenic mice

We tested the efficacy of γPNA-NLS in a transgenic mouse model with an active immune system. Eμ-myc transgenic mice mimic the t(8; 14) translocation of *c-Myc* in BL and place the murine *c-Myc* gene under the control of IgH regulatory elements.[84] The resulting overexpression of *c-Myc* leads to B cell lymphomagenesis in transgenic mice. We compared the biodistribution of fluorophore-conjugated γPNA-NLS-T after i.v. and subcutaneous (s.c.) administration in Eμ-myc mice. IVIS imaging indicated a higher accumulation of γPNA-NLS-T in the isolated lymph nodes (LNs) after s.c. dosing compared with the i.v. route at 24 h (Figure 6A). We noticed a significant TAMRA fluorescence signal in LNs and minimal accumulation in the liver after s.c. delivery (Figures 6B and S6A). These results are consistent with the reports of high lymphatic drainage after s.c. injection.[85] We observed a substantial accumulation of γPNA-NLS-T in cervical, brachial, and axillary LNs 6 h after s.c. dosing in Eμ-myc mice compared with the control group (Figure 6C). We designed γPNA4-NLS (target site: 5′-GGAAAAAGAAGGGAGGGGAGGGA-3′) complementary to the target site upstream of P2 in the mouse *Myc* locus, which differs from the human sequence, to investigate the antigene activity *in vivo*. We administered two doses of γPNA4-NLS over 2 days via the s.c. route in Eμ-myc mice to determine the short-term efficacy of inhibiting *c-Myc* (Figure 6D). We noted a moderate decrease in the mass of cervical and brachial LNs collected on day 3 in γPNA4-NLS treated Eμ-myc mice (Figure 6D). WB analysis of the lysates of cervical and brachial LNs (day 3) showed an ∼80% and ∼60% decrease in c-MYC protein in γPNA4-NLS-treated mice (Figures 6E and 6F). Similarly, axillary LNs from the treated mice showed an ∼40% reduction in c-MYC (Figures S6B and S6C). Next, we performed histological (Figure S6D) and immunohistochemical analyses of the collected LNs. We noted reduced Ki67 and increased caspase-3 staining in cervical and brachial LNs of γPNA4-NLS-treated mice (Figures 6G and S6E). Axillary LNs from the treated mice also showed a moderate decrease in Ki67 and higher caspase 3 levels

Figure 5. Efficacy of γPNA2-NLS in combination with HDACis and chemotherapeutic drugs

(A) Percentage viability of U2932 cells treated with the indicated γPNA-NLS, HDAC inhibitors, and combination at 1, 2, and 4 days.

(B) Fold change of *c-Myc* and *EZH2* gene expression in treated U2932 cells on day 4.

(C) WB analysis representing c-MYC and EZH2 protein levels in U2932 cells on day 4.

(D) Fold change in *c-Myc* and *EZH2* levels in Raji cells after 24 h.

(E) Percentage of viability of U2932 cells treated with doses of CHOP or in combination with γPNA2-NLS after 24 h.

(A, B, D, and E) Graphs show mean ± SEM (n = 3); p value for unpaired two-sample t test.

(F) Workflow representing the *in vivo* study plan to evaluate the efficacy of γPNA2-NLS with romidepsin (top) and tumor growth curve of U2932 xenografts after treatment with romidepsin and combination of romidepsin with γPNA2-NLS (bottom). Vehicle, n = 5; romidepsin, n = 8; γPNA2-NLS+romidepsin, n = 8.

(G) Representative immunohistochemistry images of H&E, Ki67, and caspase-3 staining in U2932 xenografts post survival.

(F and G) Graphs show mean ± SEM (n = 3); p value for two-way ANOVA. **p < 0.01, ***p < 0.0001.

(H) Workflow representing the *in vivo* study plan to evaluate γPNA2-NLS efficacy with CHOP (top) and tumor growth curve of U2932 xenografts treated with CHOP and γPNA2-NLS+CHOP (bottom). Control, n = 6; CHOP, n = 7; γPNA2-NLS+CHOP, n = 6.

(I) Representative immunohistochemistry images of H&E, Ki67, and caspase-3 staining in control, CHOP-, and γPNA2-NLS+CHOP-treated U2932 tumors post survival.

(G and I) Scale bars, 100 μm (H&E) and 50 μm (immunohistochemistry).

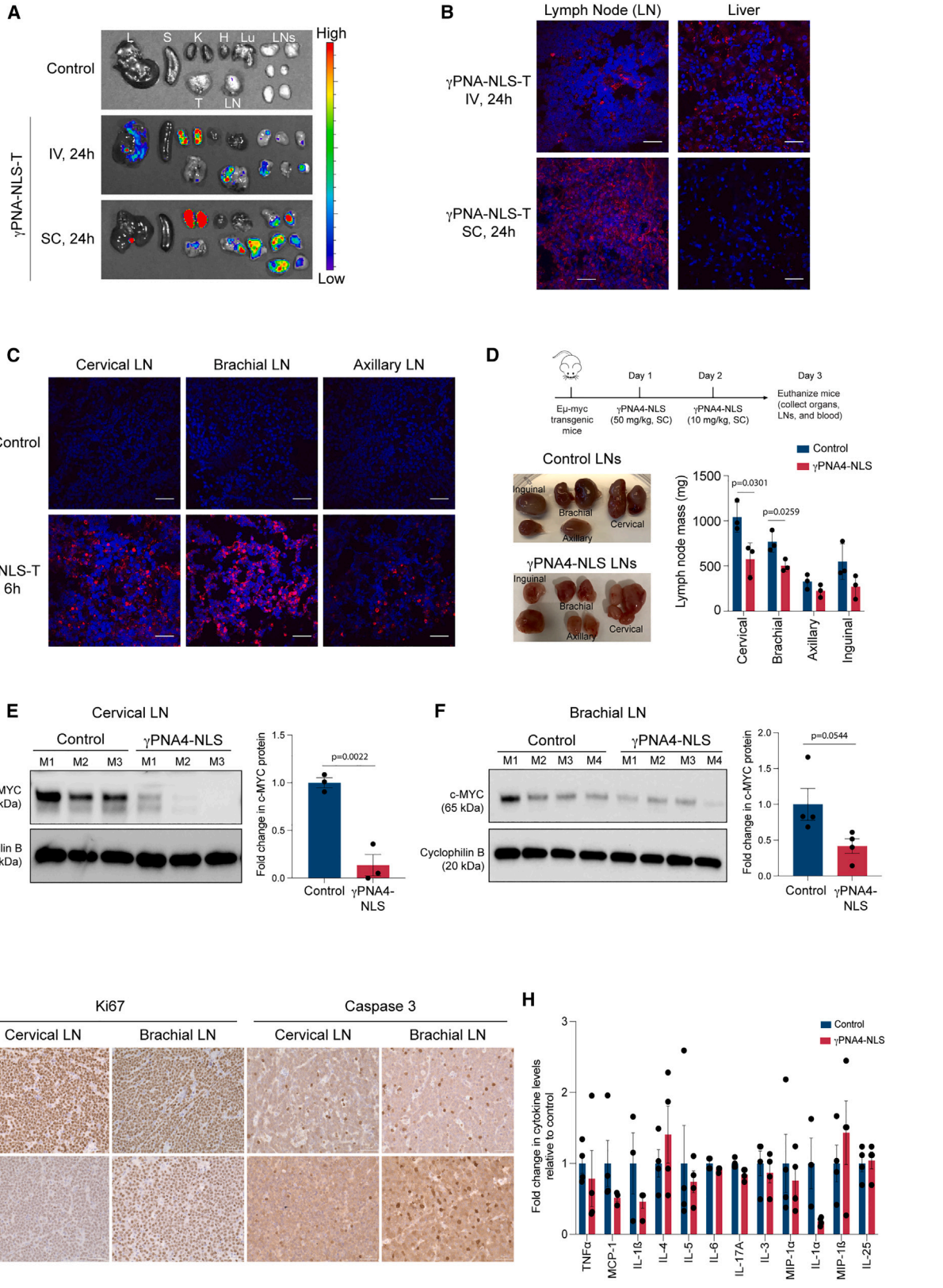

(legend on next page)

(Figure S6F). These results established that s.c. administered γPNA4-NLS could efficiently accumulate in the LNs to inhibit the proliferation of *c-Myc*-driven lymphomas. Cytokine array analysis did not indicate activation of the innate immune response in γPNA4-NLS-treated Eμ-myc mice (Figure 6H). No alteration in the histology of the organs was observed in γPNA4-NLS-treated and untreated Eμ-myc mice (Figure S6G), establishing the safety of γPNA-NLS in an immunocompetent mouse model.

To confirm the specificity of γPNA4-NLS, we treated the Eμ-myc mice with human-specific γPNA2-NLS followed by WB analysis. The lysates from the brachial and cervical LNs showed no significant difference in the c-MYC protein levels (Figures S6H and S6I). We tested the efficacy of γPNA4-NLS on U2932 cells and observed no difference in *c-Myc* gene expression (Figure S6J). These results together emphasize the site specificity of γPNA4-NLS and γPNA2-NLS to mouse and human *c-Myc* targets, respectively.

Efficacy of γPNA2-NLS in combination with romidepsin and CHOP in PDXs

We evaluated the combination of γPNA2-NLS with romidepsin and CHOP therapy in a DLBCL PDX mouse model. PDXs contain cancer stem cells and a heterogeneous cancer cell population, presenting a more rigorous platform to access therapeutic agents.[86] Two doses of romidepsin, administered via the intraperitoneal (i.p.) (1 mg/kg) route on days 0 and 6, were used to sensitize the PDX to γPNA2-NLS. We observed a 2.3- and 1.5-fold reduction in the PDX tumors treated with γPNA2-NLS (5 mg/kg) and romidepsin on day 15, respectively (Figure 7A). γPNA2-NLS- and romidepsin-treated PDX mice had 2.4-fold lower tumor volumes than those with only γPNA2-NLS or romidepsin treatment, which showed a 1.4- and 1.3-fold decrease on day 35 (Figures 7B and 7C). H&E- and Ki67-stained sections of the PDX tumors treated with the combination showed significantly higher necrosis and minimal proliferation (Figure 7D). The quantification of Ki67 staining indicated an ∼3-fold decrease in proliferation relative to individual treatments, which showed only a 1.8-fold reduction (Figure 7E). Similarly, we observed 6.4-fold higher caspase-3 activation in PDX tumors treated with γPNA2-NLS and romidepsin than tumors treated with only γPNA2-NLS or romidepsin (∼5-fold increase) (Figures S7A and S7B). We did not notice a change in mouse weight, indicating the safety of γPNA2-NLS in combination with romidepsin (Figure S7C).

Next, we tested the efficacy of γPNA2-NLS and CHOP in PDX mice. Pre-treatment of PDX mice with γPNA2-NLS sensitized the tumors toward CHOP, resulting in a 3.4-fold lower tumor volume relative to the CHOP treatment (1.9-fold) on day 15 (Figure 7F). γPNA2-NLS+CHOP-treated PDX-tumors showed 2-fold lower tumor volumes than the CHOP-only group on day 35 (Figures 7G and 7H). We noted a 3.5-fold reduction in Ki67 staining (Figures 7I and 7J) and an increase in caspase-3 activation (Figures S7D and S7E) in combination-treated PDX mice, with visible disruption of the tumors through histological analysis. More importantly, the CHOP treatment did not result in a weight decrease in the PDX mice (Figure S7F), establishing the potential of γPNA2-NLS to improve the therapeutic efficacy of CHOP at reduced clinical doses with no signs of toxicity. To confirm the specificity of the γPNA2-NLS, we tested the *in vivo* activity of Scr-γPNA3-NLS and did not observe its impact on the growth of PDX tumors after multiple dosing (Figure S7G).

To ensure the safety of γPNA-NLS, we used flow cytometry analysis to evaluate the changes in various immune cells, including $CD19^+$ B cells, $CD3^+$ T cells, $CD11b^+$ $F4/80^+$ monocytes/macrophages, $Ly6G^+$ neutrophils, and $NK1.1^+$ NK cells (Figure S7H), in an immune-competent mouse model. We observed no changes in the immune cells of C57BL/6 mice post treatment with γPNA2-NLS (25 mg/kg) (Figure S7I). Further, TAMRA-conjugated γPNA-NLS did not show uptake in $CD11b^+$ $F4/80^+$ monocytes/macrophages (Figures S7J and S7K). We performed a cytokine array in γPNA2-NLS-treated C57BL/6 mice and did not notice an increase in cytokines (Figure S7L). These results suggest a lack of immunogenic response for γPNA2-NLS administered systemically.

DISCUSSION

Targeting genomic DNA has been challenging as it is packed into chromatin, and the duplex is thermodynamically stable due to the WC base-pairing and nucleobase stacking.[6,78] It has been established that genomic DNA undergoes thermal fluctuations or breathing.[87] The breathing of genomic DNA results in the accessibility of nucleobases in the duplex to high-affinity sequence-selective DNA binders.

Prior studies have reported that modifications at the γ position in the PNA backbone pre-organize it into a right-handed helical structure.[27,28] γPNAs invade the mixed sequences of genomic DNA via WC base-pairing. It has been confirmed that the γPNAs can induce gene editing *in vivo* by targeting genomic DNA.[29,31] The progress in targeting genomic DNA for cancer therapy has not been investigated thoroughly. Few studies have explored the genomic DNA targeting features of PNAs to inhibit cancer growth.[88,89] Initial efforts were focused on unmodified PNAs to target the transcription start site (TSS) to inhibit the expression of oncogenes. Prior work has shown PNA-mediated transcription inhibition of human progesterone receptors for breast cancer[90,91]

Figure 6. Anti-transcription efficacy of γPNA-NLS in Eμ-myc transgenic mice

(A) *In vivo* biodistribution of γPNA-NLS-T (5 mg/kg) in the LNs and organs of Eμ-myc mice.

(B) Confocal images after 24 h of γPNA-NLS-T i.v. and s.c. administration.

(C) Confocal images of LNs isolated from control and γPNA-NLS-T-treated (5 mg/kg) mice after 6 h.

(B and C) Scale bars 30 μm.

(D) Workflow representing the study plan for evaluating γPNA4-NLS efficacy in Eμ-myc mice (top), representative images of the LNs from control and γPNA4-NLS-treated mice (bottom left), and graph representing the mass of LNs from control and γPNA4-NLS post treatment (bottom right).

(E and F) c-MYC protein levels in Eμ-myc mice on day 3 (left). The graph represents the protein quantification (right).

(G) Representative immunohistochemistry images from control and γPNA4-NLS-treated mice. Scale bar, 50 μm.

(H) Relative fold change in the level of cytokines in γPNA4-NLS-treated Eμ-myc mice on day 3 relative to the control group. Graph shows mean ± SEM (n = 3); p value for unpaired two-sample t test.

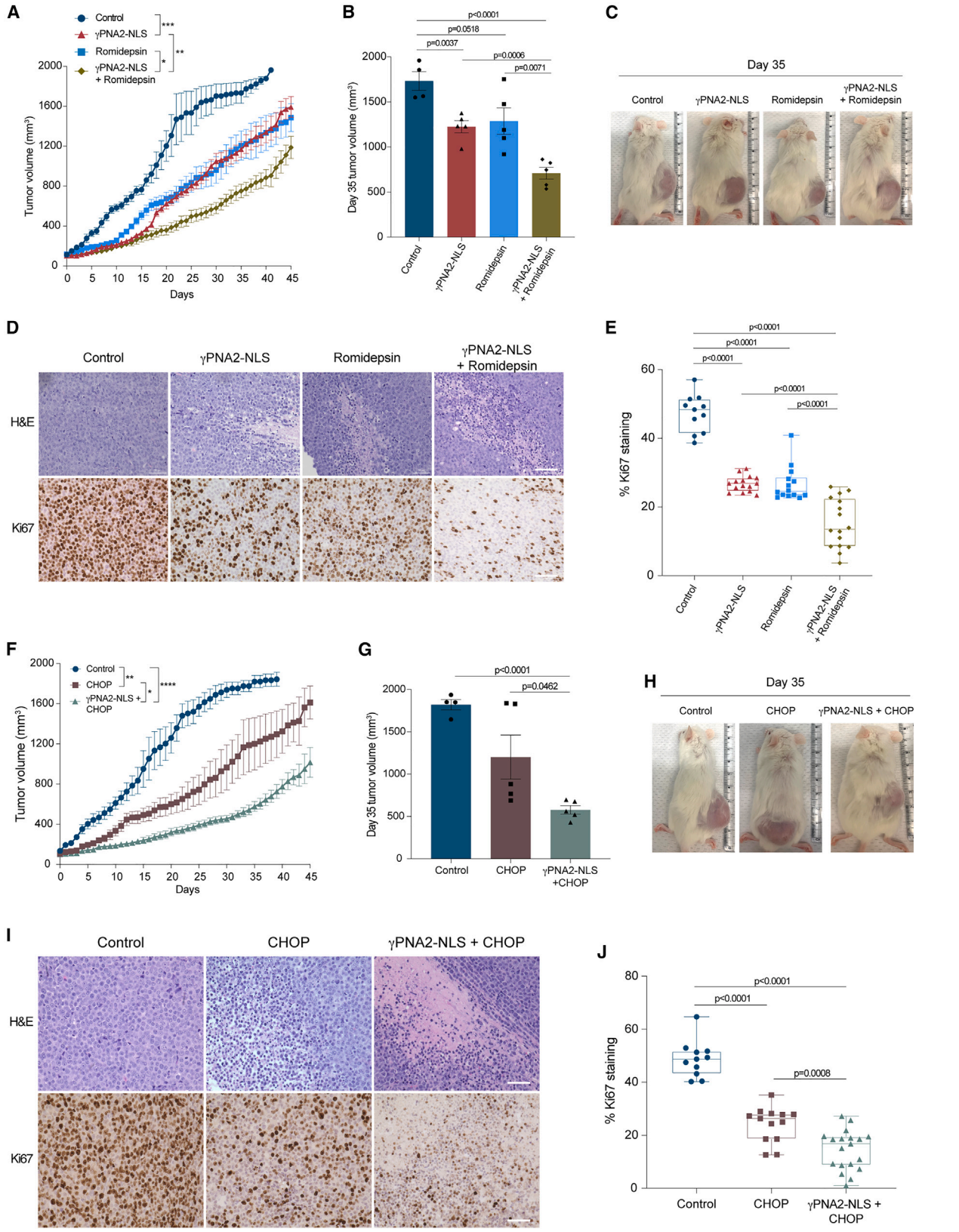

(legend on next page)

and *c-Myc* in Burkitt's lymphoma.[89] While promising, most studies were performed using cell culture-based analysis and demonstrated limited pre-clinical development.

Here, we designed γPNAs to inhibit the transcription of oncogenic *c-Myc* and comprehensively tested its efficacy and safety *in vivo*. *c-Myc* is dysregulated in more than 50% of cancers driving tumorigenesis,[40] and yet there are no *c-Myc*-specific inhibitors on the market.[92] Regular PNA, designed to target the Eμ enhancer region in BL to inhibit *c-Myc*, reduced tumor growth in a xenograft mouse model; however, it warrants further investigation.[89] We conducted pre-clinical and safety analyses of γPNAs targeting the *c-Myc* promoter region in multiple animal models. The combination of a γPNA backbone, tail-clamp design, and addition of an NLS allows the γPNA-NLS to invade the genomic DNA and form a thermodynamically stable DNA:γPNA complex to inhibit the transcription of *c-Myc in vivo*.

Cellular uptake studies revealed substantial uptake of TAMRA-conjugated γPNA-NLS in lymphoma cells. Gene expression studies in multiple lymphomas and other cancer cells established the superior efficacy of targeting P2 over P1 to inhibit transcription. Moreover, we did not notice a change in the γH2AX levels in γPNA-NLS-treated lymphoma cells, consistent with prior results.[29,93] One explanation is that γPNA-NLS invades the genomic DNA via duplex invasion, which does not induce DSBs.

In biodistribution studies, we observed passive accumulation due to the enhanced permeability and retention effect.[94] We noted a decrease in c-MYC protein after a single dose and multiple doses in U2932 xenograft and Eu-myc transgenic mice. Multiple systemic doses of γPNA2-NLS reduced the growth of three xenograft tumors. Co-treatment with γPNA2-NLS and romidepsin further improved the survival of U2932 xenograft mice. Inhibition of *c-Myc* transcription impaired DNA replication and damage response in lymphoma cells, making them more sensitive to chemotherapeutic drugs. Combining γPNA2-NLS and CHOP improved the survival of U2932 and PDX mice.

These results indicate the potential of γPNA-NLS as an anti-transcription agent for cancer therapy. Overall, we provide adequate pre-clinical data to support γPNA-NLS-based silencing of oncogenes at the genomic DNA level for cancer therapy.

Limitations of the study

We conducted proof-of-concept genomic DNA-targeting studies to inhibit *c-Myc*, potentially extending to other oncogenes commonly dysregulated in various cancers.[95–97] We tested a few targeted sites on the *c-Myc* oncogene. Advances in bioinformatic and genome sequencing tools enable screening of multiple genomic DNA sites that can potentially inhibit transcription by blocking RNA polymerase. Although we attempted to determine the off-target effects, they were not ruled out completely. Additional studies, including whole-genome sequencing and time-dependent RNA sequencing considering *c-Myc* transcript half-life, can be performed to ensure specificity. Further, the survival study in the Eμ-Myc mouse model is challenging due to the intrinsic heterogenicity in onset of B cell lymphoma.[98,99] To assess the efficacy of the γPNA-NLS-based antigene strategy, it's advisable to explore extended survival studies in Eμ-myc mice with synchronized B cell lymphoma onset. γPNA-NLS passively accumulates in the tumors and undergoes nuclear transport. *In vivo* targeting can be improved by active delivery of γPNA-NLS using ligands targeting the tumor microenvironment.[100]

STAR★METHODS

Detailed methods are provided in the online version of this paper and include the following:

- KEY RESOURCES TABLE
- RESOURCE AVAILABILITY
  - Lead contact
  - Materials availability
  - Data and code availability
- EXPERIMENTAL MODEL AND STUDY PARTICIPANT DETAILS
  - Xenograft animal model
  - Cell culture
- METHODS DETAILS
  - Synthesis of PNA oligomers
  - Gel electrophoresis
  - Cellular uptake
  - PCR amplicon assay
  - γH2AX foci assay
  - Comet assay
  - Cell viability
  - Apoptosis assay
  - Gene expression
  - RNA-sequencing
  - *In vivo* studies in xenograft mice model
  - *In vivo* studies in PDX mice

Figure 7. Efficacy of γPNA2-NLS in the DLBCL patient-derived xenograft (PDX) mouse model

(A) Tumor growth curve of DLBCL PDX mice treated with γPNA-NLS, HDACis, and combination (control, n = 4; γPNA2-NLS, n = 6; romidepsin, n = 6; γPNA2-NLS+romidepsin, n = 6).

(B) Graph representing tumor volumes of the indicated groups. Control, n = 4; γPNA2-NLS, n = 5; romidepsin, n = 5; γPNA2-NLS+romidepsin, n = 5.

(C) Representative images of mice bearing tumors from the indicated treatment groups.

(D) Representative immunohistochemistry images from different groups. Scale bar, 50 μm.

(E) Boxplot representing quantification of Ki67 in tumor sections.

(F) Tumor growth curve of mice treated with CHOP and combination of γPNA2-NLS with CHOP (control, n = 5; CHOP, n = 6; γPNA2-NLS+CHOP, n = 5).

(G) Graph representing the tumor volumes from the indicated treatment groups (control, n = 4; CHOP, n = 5; γPNA2-NLS+CHOP, n = 5).

(H) Representative images of mice bearing tumors from the indicated groups.

(I) Representative images of H&E- and Ki67-stained tumor sections Scale bar, 50 μm.

(J) Boxplot representing Ki67 quantification in tumor sections (control, n = 2; CHOP, n = 2; γPNA2-NLS+CHOP, n = 3).

Results are presented as mean ± SEM; p value for unpaired two-sample t test. For tumor growth curves: p value for two-way ANOVA. *$p < 0.05$, **$p < 0.01$, ***$p < 0.001$.

- *In vivo* studies in transgenic mice model
- Immunotoxicology studies
- Western blot analysis
- Immunohistochemistry
- Statistical analysis

SUPPLEMENTAL INFORMATION

Supplemental information can be found online at https://doi.org/10.1016/j.xcrm.2023.101354.

ACKNOWLEDGMENTS

Work in the R.B. lab was supported by an NIH, United States R01 (1R01CA241194-01A1) grant.

AUTHOR CONTRIBUTIONS

R.B. conceived the study idea. S.M., S.P.P., V.K., and J.C.V. performed experiments. Y.D., Y.X., R.F., and V.S. analyzed RNA sequencing data. R.B., S.M., S.P.P., V.K., Y.D., Y.X., and J.C.V. wrote the manuscript.

DECLARATION OF INTERESTS

The authors declare no competing interests.

Received: October 13, 2022
Revised: September 21, 2023
Accepted: December 11, 2023
Published: January 5, 2024

REFERENCES

1. Crooke, S.T., Baker, B.F., Crooke, R.M., and Liang, X.H. (2021). Antisense technology: an overview and prospectus. Nat. Rev. Drug Discov. *20*, 427–453.
2. Kulkarni, J.A., Witzigmann, D., Thomson, S.B., Chen, S., Leavitt, B.R., Cullis, P.R., and van der Meel, R. (2021). The current landscape of nucleic acid therapeutics. Nat. Nanotechnol. *16*, 630–643.
3. Li, X., Pu, W., Zheng, Q., Ai, M., Chen, S., and Peng, Y. (2022). Proteolysis-targeting chimeras (PROTACs) in cancer therapy. Mol. Cancer *21*, 99.
4. Cheung-Ong, K., Giaever, G., and Nislow, C. (2013). DNA-damaging agents in cancer chemotherapy: serendipity and chemical biology. Chem. Biol. *20*, 648–659.
5. Reimer, R.R., Hoover, R., Fraumeni, J.F., Jr., and Young, R.C. (1977). Acute leukemia after alkylating-agent therapy of ovarian cancer. N. Engl. J. Med. *297*, 177–181.
6. Travis, L.B., Holowaty, E.J., Bergfeldt, K., Lynch, C.F., Kohler, B.A., Wiklund, T., Curtis, R.E., Hall, P., Andersson, M., Pukkala, E., et al. (1999). Risk of leukemia after platinum-based chemotherapy for ovarian cancer. N. Engl. J. Med. *340*, 351–357.
7. Zhou, K., Gaullier, G., and Luger, K. (2019). Nucleosome structure and dynamics are coming of age. Nat. Struct. Mol. Biol. *26*, 3–13.
8. Yakovchuk, P., Protozanova, E., and Frank-Kamenetskii, M.D. (2006). Base-stacking and base-pairing contributions into thermal stability of the DNA double helix. Nucleic Acids Res. *34*, 564–574.
9. Belting, M., Sandgren, S., and Wittrup, A. (2005). Nuclear delivery of macromolecules: barriers and carriers. Adv. Drug Deliv. Rev. *57*, 505–527.
10. Dervan, P.B., and Edelson, B.S. (2003). Recognition of the DNA minor groove by pyrrole-imidazole polyamides. Curr. Opin. Struct. Biol. *13*, 284–299.
11. Kurmis, A.A., Yang, F., Welch, T.R., Nickols, N.G., and Dervan, P.B. (2017). A Pyrrole-Imidazole Polyamide Is Active against Enzalutamide-Resistant Prostate Cancer. Cancer Res. *77*, 2207–2212.
12. Yang, F., Nickols, N.G., Li, B.C., Marinov, G.K., Said, J.W., and Dervan, P.B. (2013). Antitumor activity of a pyrrole-imidazole polyamide. Proc. Natl. Acad. Sci. USA *110*, 1863–1868.
13. Kelly, J.J., Baird, E.E., and Dervan, P.B. (1996). Binding site size limit of the 2:1 pyrrole-imidazole polyamide-DNA motif. Proc. Natl. Acad. Sci. USA *93*, 6981–6985.
14. Knauert, M.P., and Glazer, P.M. (2001). Triplex forming oligonucleotides: sequence-specific tools for gene targeting. Hum. Mol. Genet. *10*, 2243–2251.
15. Catapano, C.V., McGuffie, E.M., Pacheco, D., and Carbone, G.M. (2000). Inhibition of gene expression and cell proliferation by triple helix-forming oligonucleotides directed to the c-myc gene. Biochemistry *39*, 5126–5138.
16. Cooney, M., Czernuszewicz, G., Postel, E.H., Flint, S.J., and Hogan, M.E. (1988). Site-specific oligonucleotide binding represses transcription of the human c-myc gene in vitro. Science *241*, 456–459.
17. Faria, M., Wood, C.D., Perrouault, L., Nelson, J.S., Winter, A., White, M.R., Helene, C., and Giovannangeli, C. (2000). Targeted inhibition of transcription elongation in cells mediated by triplex-forming oligonucleotides. Proc. Natl. Acad. Sci. USA *97*, 3862–3867.
18. McGuffie, E.M., Pacheco, D., Carbone, G.M., and Catapano, C.V. (2000). Antigene and antiproliferative effects of a c-myc-targeting phosphorothioate triple helix-forming oligonucleotide in human leukemia cells. Cancer Res. *60*, 3790–3799.
19. Egholm, M., Buchardt, O., Christensen, L., Behrens, C., Freier, S.M., Driver, D.A., Berg, R.H., Kim, S.K., Norden, B., and Nielsen, P.E. (1993). PNA hybridizes to complementary oligonucleotides obeying the Watson-Crick hydrogen-bonding rules. Nature *365*, 566–568.
20. Nielsen, P.E., Egholm, M., Berg, R.H., and Buchardt, O. (1991). Sequence-selective recognition of DNA by strand displacement with a thymine-substituted polyamide. Science *254*, 1497–1500.
21. Demidov, V.V., Potaman, V.N., Frank-Kamenetskii, M.D., Egholm, M., Buchard, O., Sönnichsen, S.H., and Nielsen, P.E. (1994). Stability of peptide nucleic acids in human serum and cellular extracts. Biochem. Pharmacol. *48*, 1310–1313.
22. Betts, L., Josey, J.A., Veal, J.M., and Jordan, S.R. (1995). A nucleic acid triple helix formed by a peptide nucleic acid-DNA complex. Science *270*, 1838–1841.
23. Lohse, J., Dahl, O., and Nielsen, P.E. (1999). Double duplex invasion by peptide nucleic acid: a general principle for sequence-specific targeting of double-stranded DNA. Proc. Natl. Acad. Sci. USA *96*, 11804–11808.
24. Egholm, M., Christensen, L., Dueholm, K.L., Buchardt, O., Coull, J., and Nielsen, P.E. (1995). Efficient pH-independent sequence-specific DNA binding by pseudoisocytosine-containing bis-PNA. Nucleic Acids Res. *23*, 217–222.
25. Bentin, T., Larsen, H.J., and Nielsen, P.E. (2003). Combined triplex/duplex invasion of double-stranded DNA by "tail-clamp" peptide nucleic acid. Biochemistry *42*, 13987–13995.
26. Kaihatsu, K., Shah, R.H., Zhao, X., and Corey, D.R. (2003). Extending recognition by peptide nucleic acids (PNAs): binding to duplex DNA and inhibition of transcription by tail-clamp PNA-peptide conjugates. Biochemistry *42*, 13996–14003.
27. Dragulescu-Andrasi, A., Rapireddy, S., Frezza, B.M., Gayathri, C., Gil, R.R., and Ly, D.H. (2006). A simple gamma-backbone modification preorganizes peptide nucleic acid into a helical structure. J. Am. Chem. Soc. *128*, 10258–10267.
28. He, G., Rapireddy, S., Bahal, R., Sahu, B., and Ly, D.H. (2009). Strand invasion of extended, mixed-sequence B-DNA by gammaPNAs. J. Am. Chem. Soc. *131*, 12088–12090.

29. Bahal, R., Ali McNeer, N., Quijano, E., Liu, Y., Sulkowski, P., Turchick, A., Lu, Y.C., Bhunia, D.C., Manna, A., Greiner, D.L., et al. (2016). In vivo correction of anaemia in beta-thalassemic mice by gammaPNA-mediated gene editing with nanoparticle delivery. Nat. Commun. *7*, 13304.

30. Malik, S., Oyaghire, S., and Bahal, R. (2019). Applications of PNA-laden nanoparticles for hematological disorders. Cell. Mol. Life Sci. *76*, 1057–1065.

31. Ricciardi, A.S., Bahal, R., Farrelly, J.S., Quijano, E., Bianchi, A.H., Luks, V.L., Putman, R., López-Giráldez, F., Coşkun, S., Song, E., et al. (2018). In utero nanoparticle delivery for site-specific genome editing. Nat. Commun. *9*, 2481.

32. Meyer, N., and Penn, L.Z. (2008). Reflecting on 25 years with MYC. Nat. Rev. Cancer *8*, 976–990.

33. Nesbit, C.E., Tersak, J.M., and Prochownik, E.V. (1999). MYC oncogenes and human neoplastic disease. Oncogene *18*, 3004–3016.

34. Ott, G., Rosenwald, A., and Campo, E. (2013). Understanding MYC-driven aggressive B-cell lymphomas: pathogenesis and classification. Blood *122*, 3884–3891.

35. Jin, F., Yu, C., Lai, L., and Liu, Z. (2013). Ligand clouds around protein clouds: a scenario of ligand binding with intrinsically disordered proteins. PLoS Comput. Biol. *9*, e1003249.

36. Choi, S.H., Mahankali, M., Lee, S.J., Hull, M., Petrassi, H.M., Chatterjee, A.K., Schultz, P.G., Jones, K.A., and Shen, W. (2017). Targeted Disruption of Myc-Max Oncoprotein Complex by a Small Molecule. ACS Chem. Biol. *12*, 2715–2719.

37. Struntz, N.B., Chen, A., Deutzmann, A., Wilson, R.M., Stefan, E., Evans, H.L., Ramirez, M.A., Liang, T., Caballero, F., Wildschut, M.H.E., et al. (2019). Stabilization of the Max Homodimer with a Small Molecule Attenuates Myc-Driven Transcription. Cell Chem. Biol. *26*, 711–723.e14.

38. Hart, J.R., Garner, A.L., Yu, J., Ito, Y., Sun, M., Ueno, L., Rhee, J.K., Baksh, M.M., Stefan, E., Hartl, M., et al. (2014). Inhibitor of MYC identified in a Krohnke pyridine library. Proc. Natl. Acad. Sci. USA *111*, 12556–12561.

39. Pillai, R. (1991). Oncogene expression and prognosis in cervical cancer. Cancer Lett. *59*, 171–175.

40. Chen, H., Liu, H., and Qing, G. (2018). Targeting oncogenic Myc as a strategy for cancer treatment. Signal Transduct. Targeted Ther. *3*, 5.

41. Beaulieu, M.E., Jauset, T., Massó-Vallés, D., Martínez-Martín, S., Rahl, P., Maltais, L., Zacarias-Fluck, M.F., Casacuberta-Serra, S., Serrano Del Pozo, E., Fiore, C., et al. (2019). Intrinsic cell-penetrating activity propels Omomyc from proof of concept to viable anti-MYC therapy. Sci. Transl. Med. *11*, eaar5012.

42. Brooks, T.A., and Hurley, L.H. (2010). Targeting MYC Expression through G-Quadruplexes. Genes Cancer *1*, 641–649.

43. Webb, M.S., Tortora, N., Cremese, M., Kozlowska, H., Blaquiere, M., Devine, D.V., and Kornbrust, D.J. (2001). Toxicity and toxicokinetics of a phosphorothioate oligonucleotide against the c-myc oncogene in cynomolgus monkeys. Antisense Nucleic Acid Drug Dev. *11*, 155–163.

44. Sklar, M.D., Thompson, E., Welsh, M.J., Liebert, M., Harney, J., Grossman, H.B., Smith, M., and Prochownik, E.V. (1991). Depletion of c-myc with specific antisense sequences reverses the transformed phenotype in ras oncogene-transformed NIH 3T3 cells. Mol. Cell Biol. *11*, 3699–3710.

45. Wickstrom, E., Bacon, T.A., Wickstrom, E.L., Werking, C.M., Palmiter, R.D., Brinster, R.L., and Sandgren, E.P. (1991). Antisense oligodeoxynucleoside methylphosphonate inhibition of mouse c-myc p65 protein expression in E mu-c-myc transgenic mice. Nucleic Acids Symp. Ser. *1991*, 151–154.

46. Kabilova, T.O., Chernolovskaya, E.L., Vladimirova, A.V., and Vlassov, V.V. (2006). Inhibition of human carcinoma and neuroblastoma cell proliferation by anti-c-myc siRNA. Oligonucleotides *16*, 15–25.

47. Shen, L., Zhang, C., Ambrus, J.L., and Wang, J.H. (2005). Silencing of human c-myc oncogene expression by poly-DNP-RNA. Oligonucleotides *15*, 23–35.

48. Bayat Mokhtari, R., Homayouni, T.S., Baluch, N., Morgatskaya, E., Kumar, S., Das, B., and Yeger, H. (2017). Combination therapy in combating cancer. Oncotarget *8*, 38022–38043.

49. Hontecillas-Prieto, L., Flores-Campos, R., Silver, A., de Álava, E., Hajji, N., and García-Domínguez, D.J. (2020). Synergistic Enhancement of Cancer Therapy Using HDAC Inhibitors: Opportunity for Clinical Trials. Front. Genet. *11*, 578011.

50. Boxer, L.M., and Dang, C.V. (2001). Translocations involving c-myc and c-myc function. Oncogene *20*, 5595–5610.

51. Battey, J., Moulding, C., Taub, R., Murphy, W., Stewart, T., Potter, H., Lenoir, G., and Leder, P. (1983). The human c-myc oncogene: structural consequences of translocation into the IgH locus in Burkitt lymphoma. Cell *34*, 779–787.

52. Spencer, C.A., and Groudine, M. (1991). Control of c-myc regulation in normal and neoplastic cells. Adv. Cancer Res. *56*, 1–48.

53. Taub, R., Moulding, C., Battey, J., Murphy, W., Vasicek, T., Lenoir, G.M., and Leder, P. (1984). Activation and somatic mutation of the translocated c-myc gene in burkitt lymphoma cells. Cell *36*, 339–348.

54. Roussel, M.F., Davis, J.N., Cleveland, J.L., Ghysdael, J., and Hiebert, S.W. (1994). Dual control of myc expression through a single DNA binding site targeted by ets family proteins and E2F-1. Oncogene *9*, 405–415.

55. Bossone, S.A., Asselin, C., Patel, A.J., and Marcu, K.B. (1992). MAZ, a zinc finger protein, binds to c-MYC and C2 gene sequences regulating transcriptional initiation and termination. Proc. Natl. Acad. Sci. USA *89*, 7452–7456.

56. Christensen, L., Fitzpatrick, R., Gildea, B., Petersen, K.H., Hansen, H.F., Koch, T., Egholm, M., Buchardt, O., Nielsen, P.E., Coull, J., and Berg, R.H. (1995). Solid-phase synthesis of peptide nucleic acids. J. Pept. Sci. *1*, 175–183.

57. Brandén, L.J., Mohamed, A.J., and Smith, C.I. (1999). A peptide nucleic acid-nuclear localization signal fusion that mediates nuclear transport of DNA. Nat. Biotechnol. *17*, 784–787.

58. Malik, S., Lim, J., Slack, F.J., Braddock, D.T., and Bahal, R. (2020). Next generation miRNA inhibition using short anti-seed PNAs encapsulated in PLGA nanoparticles. J. Contr. Release *327*, 406–419.

59. Li, W., Gupta, S.K., Han, W., Kundson, R.A., Nelson, S., Knutson, D., Greipp, P.T., Elsawa, S.F., Sotomayor, E.M., and Gupta, M. (2019). Targeting MYC activity in double-hit lymphoma with MYC and BCL2 and/or BCL6 rearrangements with epigenetic bromodomain inhibitors. J. Hematol. Oncol. *12*, 73.

60. Lue, J.K., and Amengual, J.E. (2018). Emerging EZH2 Inhibitors and Their Application in Lymphoma. Curr. Hematol. Malig. Rep. *13*, 369–382.

61. Kaur, M., and Cole, M.D. (2013). MYC acts via the PTEN tumor suppressor to elicit autoregulation and genome-wide gene repression by activation of the Ezh2 methyltransferase. Cancer Res. *73*, 695–705.

62. Sander, S., Bullinger, L., Klapproth, K., Fiedler, K., Kestler, H.A., Barth, T.F.E., Möller, P., Stilgenbauer, S., Pollack, J.R., and Wirth, T. (2008). MYC stimulates EZH2 expression by repression of its negative regulator miR-26a. Blood *112*, 4202–4212.

63. Strobl, L.J., Kohlhuber, F., Mautner, J., Polack, A., and Eick, D. (1993). Absence of a paused transcription complex from the c-myc P2 promoter of the translocation chromosome in Burkitt's lymphoma cells: implication for the c-myc P1/P2 promoter shift. Oncogene *8*, 1437–1447.

64. Szklarczyk, D., Gable, A.L., Lyon, D., Junge, A., Wyder, S., Huerta-Cepas, J., Simonovic, M., Doncheva, N.T., Morris, J.H., Bork, P., et al. (2019). STRING v11: protein-protein association networks with increased coverage, supporting functional discovery in genome-wide experimental datasets. Nucleic Acids Res. *47*, D607–D613.

65. Costanzo, V. (2011). Brca2, Rad51 and Mre11: performing balancing acts on replication forks. DNA Repair *10*, 1060–1065.

66. Symington, L.S. (2002). Role of RAD52 epistasis group genes in homologous recombination and double-strand break repair. Microbiol. Mol. Biol. Rev. *66*, 630–670.

67. George, T., Wen, Q., Griffiths, R., Ganesh, A., Meuth, M., and Sanders, C.M. (2009). Human Pif1 helicase unwinds synthetic DNA structures resembling stalled DNA replication forks. Nucleic Acids Res. *37*, 6491–6502.

68. Byrd, A.K., and Raney, K.D. (2017). Structure and function of Pif1 helicase. Biochem. Soc. Trans. *45*, 1159–1171.

69. Azenha, D., Lopes, M.C., and Martins, T.C. (2019). Claspin: From replication stress and DNA damage responses to cancer therapy. Adv. Protein Chem. Struct. Biol. *115*, 203–246.

70. Gari, K., Décaillet, C., Delannoy, M., Wu, L., and Constantinou, A. (2008). Remodeling of DNA replication structures by the branch point translocase FANCM. Proc. Natl. Acad. Sci. USA *105*, 16107–16112.

71. Taylor, E.M., and Lindsay, H.D. (2016). DNA replication stress and cancer: cause or cure? Future Oncol. *12*, 221–237.

72. Wang, M., Chen, S., and Ao, D. (2021). Targeting DNA repair pathway in cancer: Mechanisms and clinical application. MedComm *2*, 654–691.

73. Uzor, S., Porazinski, S.R., Li, L., Clark, B., Ajiro, M., Iida, K., Hagiwara, M., Alqasem, A.A., Perks, C.M., Wilson, I.D., et al. (2021). CDC2-like (CLK) protein kinase inhibition as a novel targeted therapeutic strategy in prostate cancer. Sci. Rep. *11*, 7963.

74. Gao, Y., Feng, B., Lu, L., Han, S., Chu, X., Chen, L., and Wang, R. (2017). MiRNAs and E2F3: a complex network of reciprocal regulations in human cancers. Oncotarget *8*, 60624–60639.

75. Zhu, X., Liao, Y., and Tang, L. (2020). Targeting BRD9 for Cancer Treatment: A New Strategy. OncoTargets Ther. *13*, 13191–13200.

76. Wu, D., Jin, J., Qiu, Z., Liu, D., and Luo, H. (2020). Functional Analysis of O-GlcNAcylation in Cancer Metastasis. Front. Oncol. *10*, 585288.

77. Yendamuri, S., Trapasso, F., and Calin, G.A. (2008). ARLTS1 - a novel tumor suppressor gene. Cancer Lett. *264*, 11–20.

78. Parmar, J.J., and Padinhateeri, R. (2020). Nucleosome positioning and chromatin organization. Curr. Opin. Struct. Biol. *64*, 111–118.

79. Li, B., Carey, M., and Workman, J.L. (2007). The role of chromatin during transcription. Cell *128*, 707–719.

80. Dawson, M.A., and Kouzarides, T. (2012). Cancer epigenetics: from mechanism to therapy. Cell *150*, 12–27.

81. Suraweera, A., O'Byrne, K.J., and Richard, D.J. (2018). Combination Therapy With Histone Deacetylase Inhibitors (HDACi) for the Treatment of Cancer: Achieving the Full Therapeutic Potential of HDACi. Front. Oncol. *8*, 92.

82. Marchion, D.C., Bicaku, E., Daud, A.I., Sullivan, D.M., and Munster, P.N. (2005). Valproic acid alters chromatin structure by regulation of chromatin modulation proteins. Cancer Res. *65*, 3815–3822.

83. Zhang, Z., Pan, T., Liu, C., Shan, X., Xu, Z., Hong, H., Lin, H., Chen, J., and Sun, H. (2021). Cyclophosphamide induced physiological and biochemical changes in mice with an emphasis on sensitivity analysis. Ecotoxicol. Environ. Saf. *211*, 111889.

84. Harris, A.W., Pinkert, C.A., Crawford, M., Langdon, W.Y., Brinster, R.L., and Adams, J.M. (1988). The E mu-myc transgenic mouse. A model for high-incidence spontaneous lymphoma and leukemia of early B cells. J. Exp. Med. *167*, 353–371.

85. Harivardhan Reddy, L., Sharma, R.K., Chuttani, K., Mishra, A.K., and Murthy, R.S.R. (2005). Influence of administration route on tumor uptake and biodistribution of etoposide loaded solid lipid nanoparticles in Dalton's lymphoma tumor bearing mice. J. Contr. Release *105*, 185–198.

86. Zhang, L., Nomie, K., Zhang, H., Bell, T., Pham, L., Kadri, S., Segal, J., Li, S., Zhou, S., Santos, D., et al. (2017). B-Cell Lymphoma Patient-Derived Xenograft Models Enable Drug Discovery and Are a Platform for Personalized Therapy. Clin. Cancer Res. *23*, 4212–4223.

87. Frank-Kamenetskii, M. (1987). DNA chemistry. How the double helix breathes. Nature *328*, 17–18.

88. Cutrona, G., Carpaneto, E.M., Ulivi, M., Roncella, S., Landt, O., Ferrarini, M., and Boffa, L.C. (2000). Effects in live cells of a c-myc anti-gene PNA linked to a nuclear localization signal. Nat. Biotechnol. *18*, 300–303.

89. Boffa, L.C., Cutrona, G., Cilli, M., Matis, S., Damonte, G., Mariani, M.R., Millo, E., Moroni, M., Roncella, S., Fedeli, F., and Ferrarini, M. (2007). Inhibition of Burkitt's lymphoma cells growth in SCID mice by a PNA specific for a regulatory sequence of the translocated c-myc. Cancer Gene Ther. *14*, 220–226.

90. Hu, J., and Corey, D.R. (2007). Inhibiting gene expression with peptide nucleic acid (PNA)–peptide conjugates that target chromosomal DNA. Biochemistry *46*, 7581–7589.

91. Janowski, B.A., Kaihatsu, K., Huffman, K.E., Schwartz, J.C., Ram, R., Hardy, D., Mendelson, C.R., and Corey, D.R. (2005). Inhibiting transcription of chromosomal DNA with antigene peptide nucleic acids. Nat. Chem. Biol. *1*, 210–215.

92. Whitfield, J.R., Beaulieu, M.E., and Soucek, L. (2017). Strategies to Inhibit Myc and Their Clinical Applicability. Front. Cell Dev. Biol. *5*, 10.

93. McNeer, N.A., Anandalingam, K., Fields, R.J., Caputo, C., Kopic, S., Gupta, A., Quijano, E., Polikoff, L., Kong, Y., Bahal, R., et al. (2015). Nanoparticles that deliver triplex-forming peptide nucleic acid molecules correct F508del CFTR in airway epithelium. Nat. Commun. *6*, 6952.

94. Matsumura, Y., and Maeda, H. (1986). A new concept for macromolecular therapeutics in cancer chemotherapy: mechanism of tumoritropic accumulation of proteins and the antitumor agent smancs. Cancer Res. *46*, 6387–6392.

95. Huang, L., Guo, Z., Wang, F., and Fu, L. (2021). KRAS mutation: from undruggable to druggable in cancer. Signal Transduct. Targeted Ther. *6*, 386.

96. Cocco, E., Lopez, S., Santin, A.D., and Scaltriti, M. (2019). Prevalence and role of HER2 mutations in cancer. Pharmacol. Ther. *199*, 188–196.

97. Jin, W. (2020). Role of JAK/STAT3 Signaling in the Regulation of Metastasis, the Transition of Cancer Stem Cells, and Chemoresistance of Cancer by Epithelial-Mesenchymal Transition. Cells *9*.

98. Mori, S., Rempel, R.E., Chang, J.T., Yao, G., Lagoo, A.S., Potti, A., Bild, A., and Nevins, J.R. (2008). Utilization of pathway signatures to reveal distinct types of B lymphoma in the Emicro-myc model and human diffuse large B-cell lymphoma. Cancer Res. *68*, 8525–8534.

99. Rempel, R.E., Jiang, X., Fullerton, P., Tan, T.Z., Ye, J., Lau, J.A., Mori, S., Chi, J.T., Nevins, J.R., and Friedman, D.R. (2014). Utilization of the Emu-Myc mouse to model heterogeneity of therapeutic response. Mol. Cancer Therapeut. *13*, 3219–3229.

100. Danhier, F., Feron, O., and Préat, V. (2010). To exploit the tumor microenvironment: Passive and active tumor targeting of nanocarriers for anticancer drug delivery. J. Contr. Release *148*, 135–146.

101. Love, M.I., Huber, W., and Anders, S. (2014). Moderated estimation of fold change and dispersion for RNA-seq data with DESeq2. Genome Biol. *15*, 550.

102. Yu, G., Wang, L.G., Han, Y., and He, Q.Y. (2012). clusterProfiler: an R package for comparing biological themes among gene clusters. OMICS *16*, 284–287.

STAR★METHODS

KEY RESOURCES TABLE

REAGENT or RESOURCE	SOURCE	IDENTIFIER
Antibodies		
anti-γH2AX antibody	Cell signaling technology	Cat# 9718S; RRID: AB_2118009
anti-c-MYC Rabbit mAb	Cell signaling technology	Cat# 5605; RRID:AB_1903938
anti-EZH2 Rabbit mAb	Cell signaling technology	Cat# 5246; RRID:AB_10694683
anti-Cyclophilin B Rabbit mAb	Cell signaling technology	Cat# 43603; RRID:AB_2799247
anti-β-actin Rabbit mAb	Cell signaling technology	Cat# 4970; RRID:AB_2223172
anti-rabbit IgG HRP linked antibody	Cell signaling technology	Cat# 7074; RRID:AB_2099233
anti-Ki-67 Rabbit mAb	Cell signaling technology	Cat# 9027S; RRID:AB_2636984
anti-caspase 3 Rabbit mAb	Cell signaling technology	Cat# 14214S; RRID:AB_2798426
ImPRESS HRP–polymer horse anti-rabbit secondary antibody	Vector laboratories	Cat# MP-7401: RRID:AB_2336529
anti-γH2AX antibody- PE	BioLegend	Cat# 613412; RRID:AB_2616871
anti-mouse CD3e Antibody	BD Biosciences	Cat# 563565: RRID:AB_2738278
anti-mouse NK-1.1 Antibody	BD Biosciences	Cat# 563220; RRID:AB_2738077
anti-mouse F4/80 Antibody	Biolegend	Cat# 123119; RRID:AB_893491
anti-mouse CD19 Antibody	Biolegend	Cat# 115519; RRID:AB_313655
anti-mouse/human CD11b Antibody	Biolegend	Cat# 101211; RRID:AB_312794
anti-mouse Ly-6G Antibody	Biolegend	Cat# 127623; RRID:AB_10645331
Biological samples		
Patient-derived xenografts (PDX)	diffuse large B-cell lymphoma, Patient ID 769687, specimen ID 267-B	National Cancer Institute.
Chemicals, peptides, and recombinant proteins		
Valproic acid	SelleckChem	Cat# S3944
Vorinostat	SelleckChem	Cat# ORB322396
Romidepsin	SelleckChem	Cat# ORB759987
Bleomycin	Sigma-Aldrich	Cat# B7216
Cyclophosphamide monohydrate	Sigma-Aldrich	Cat# C0768
Vincristine sulfate	Sigma-Aldrich	Cat# V0400000
Doxorubicin hydrochloride	Sigma-Aldrich	Cat# D2975000
Prednisone	Sigma-Aldrich	Cat# P26254
Dispase	Stem cell technologies	Cat# 100-0396
Collagenase	Worthington	Cat# LS004194
Mouse cell depletion cocktail	Miltenyi Biotec	Cat# 130-104-694
ProLong™ Diamond Antifade Mountant	Invitrogen	Cat# P36961
FITC Annexin V	BD Biosciences	Cat# 560931
Annexin V binding buffer	BD Biosciences	Cat# 556454
7-amino-actinomycin (7AAD)	BD Biosciences	Cat# 559925
Trypan blue	Biorad	Cat# 1450003
LIVE/DEAD™ Fixable Aqua Dead	Thermo Fisher	Cat# L34957
10x PCR reaction buffer	Sigma	Cat# P2317
10mM NTP	Invitrogen	Cat# 18427-013
DNA Taq polymerase	Promega	Cat# M300F
Glycogen	Invitrogen	Cat# AM9510
SYBR gold nucleic acid gel stain	Invitrogen	Cat# S11494
Ethidium bromide	Biorad	Cat# 1610433

(*Continued on next page*)

Continued

REAGENT or RESOURCE	SOURCE	IDENTIFIER
Agarose	Thermofisher Scientific	Cat# J32802-22
16% Paraformaldehyde	Thermofisher Scientific	Cat# 28908
Tissue plus O.C.T compound	Thermofisher Scientific	Cat# 4585
Triton X-100 (1%)	Thermofisher Scientific	Cat# HFH10
10% neutral buffered formalin	Thermofisher Scientific	Cat# SF100-4
RBC lysis buffer	Invitrogen	Cat# 00-4333-57
DC protein assay	Bio-Rad, USA	Cat# 5000112
HRP substrate	Millipore sigma, USA	Cat#WBKLS0500
TaqMan™ Gene Expression Assay (FAM) Inventoried human *c-Myc* (Hs00153408)	Thermofisher Scientific	Cat# 4331182
TaqMan™ Gene Expression Assay (FAM) Inventoried human *EZH2* (Hs00544830)	Thermofisher Scientific	Cat# 4331182
TaqMan™ Gene Expression Assay (FAM) Inventoried human *GAPDH* (Hs02758991)	Thermofisher Scientific	Cat# 4331182
TaqMan™ Gene Expression Assay (FAM) Inventoried human *BRCA2* (Hs00609073)	Thermofisher Scientific	Cat# 4331182
TaqMan™ Gene Expression Assay (FAM) Inventoried human *RAD52* (Hs01028879)	Thermofisher Scientific	Cat# 4331182
TaqMan™ Gene Expression Assay (FAM) Inventoried human *LIG4* (Hs01866071)	Thermofisher Scientific	Cat# 4331182
TaqMan™ Gene Expression Assay (FAM) Inventoried human *XRCC2* (Hs03044154)	Thermofisher Scientific	Cat# 4331182
TaqMan™ Gene Expression Assay (FAM) Inventoried human *PIF1* (Hs00228104)	Thermofisher Scientific	Cat# 4331182
TaqMan™ Gene Expression Assay (FAM) Inventoried human *CLSPN* (Hs08898637)	Thermofisher Scientific	Cat# 4331182
TaqMan™ Gene Expression Assay (FAM) Inventoried human *FANCM* (Hs00913609)	Thermofisher Scientific	Cat# 4331182
TaqMan™ Gene Expression Assay (FAM) Inventoried human *CLK1* (Hs00964634)	Thermofisher Scientific	Cat# 4331182
TaqMan™ Gene Expression Assay (FAM) Inventoried human *CLK2* (Hs02562748)	Thermofisher Scientific	Cat# 4331182
TaqMan™ Gene Expression Assay (FAM) Inventoried human *CLK4* (Hs00252917)	Thermofisher Scientific	Cat# 4331182
TaqMan™ Gene Expression Assay (FAM) Inventoried human *SRSF10* (Hs00986049)	Thermofisher Scientific	Cat# 4331182
TaqMan™ Gene Expression Assay (FAM) Inventoried human *E2F3* (Hs00605457)	Thermofisher Scientific	Cat# 4331182
TaqMan™ Gene Expression Assay (FAM) Inventoried human *BRD9* (Hs01079464)	Thermofisher Scientific	Cat# 4331182
TaqMan™ Gene Expression Assay (FAM) Inventoried human *EIF5B* (Hs01019800)	Thermofisher Scientific	Cat# 4331182
TaqMan™ Gene Expression Assay (FAM) Inventoried human *EIF4EBP* (Hs00358624)	Thermofisher Scientific	Cat# 4331182
TaqMan™ Gene Expression Assay (FAM) Inventoried human *ARL11* (Hs01936475)	Thermofisher Scientific	Cat# 4331182
TaqMan™ Gene Expression Assay (FAM) Inventoried human *OGT* (Hs00269228)	Thermofisher Scientific	Cat# 4331182
BOC-PNA-T-OH	ASM Research Chemicals	5004007
BOC-PNA-G(Cbz)-OH	ASM Research Chemicals	5004010
BOC-PNA-A(Cbz)-OH	ASM Research Chemicals	5004009
BOC-PNA-C(Cbz)-OH	ASM Research Chemicals	5004008
Boc-MiniPEG-3	Peptides International	BXX-5523-PI

(*Continued on next page*)

Continued

REAGENT or RESOURCE	SOURCE	IDENTIFIER
5-Carboxytetramethylrhodamine (TAMRA)	VWR International	91809-66-4
Critical commercial assays		
Wizard SV genomic DNA purification kit	Promega, USA	A2361
QIAquick PCR purification kit	Qiagen, USA	28106
CometAssay® kit	R&D systems	4250-050-K
Qiagen RNeasy mini kit	Qiagen, USA	74106
High capacity cDNA reverse transcription	Applied Biosystem, USA	4368814
Mmag luminex assay 16 plex	R&D systems	LXSAMSM16
Deposited data		
Raw and analyzed RNA seq Data	This paper	GEO: GSE246439
Experimental models: Cell lines		
Human: HeLa	ATCC (USA)	CCL-2
Human: A549	ATCC (USA)	CCL-185
Human: HEPG2	ATCC (USA)	HB-8065
Human: MDA-MB-231	ATCC (USA)	HTB-26
Human: PC3	ATCC (USA)	CRL-1435
Human: Raji	ATCC (USA)	CCL-86
Human: Daudi	ATCC (USA)	CCL-213
Human: U2932	DSMZ (Germany)	ACC 633
Experimental models: Organisms/strains		
Mouse: NOD.Cg-Prkdcscid Il2rgtm1Wjl/SzJ	The Jackson Laboratory	005557
Mouse: B6.Cg-Tg(IgHMyc)22Bri/J	The Jackson Laboratory	002728
Oligonucleotides		
siRNA targeting *c-myc*	Invitrogen	VHS40785
Primers amplicon assay: Forward: 5′ AGGGC TTCTCAGAGGCTTG 3′ Reverse: 5′ TGCCTCTCGCTGGAATTACT 3′	Keck Oligonucleotide Synthesis facility	N/A
dsDNA1 primer - Forward: 5′CTCTGCTTTGGGA ACCCGGGAGGGGCGCTTATGGGGAGGGTG GGGAGGG TGGGGAAGGTGGGGA 3′ Reverse: 5′AGAGTGCTCGGCTGCCCGG CTGATGTCTCTTCCCCACTCCCCACCTTCCCC ACCCTCCCCACCC 3′	Keck Oligonucleotide Synthesis facility	N/A
dsDNA2 primer - Forward: 5′TCCTGCCTCGAGAA GGGCAGGGCTTCTCAGAGGCTTGGCGGGAAAA AGA ACGGAGGGAGGGA 3′ Reverse: 5′AGATAAAGCCCCGAAAACCGGCTTTTATA CTCAGCGCGATCCCTCCCTCC GTTCTTTTTCCC 3′	Keck Oligonucleotide Synthesis facility	N/A
Software and algorithms		
FlowJo 10.8.1.	FlowJo, LLC	N/A
GraphPad Prism 9	GraphPad software	N/A
ImageJ	National Institute of Health	N/A
DESeq2 (1.30.1)	Bioconductor	N/A
ClusterProfiler (3.18.1)	Bioconductor	N/A
Cytoscape 3.9.1	Cytoscape	N/A
GSEA (Linux_4.1.0)	Broad Institute	N/A
Other		
RP-HPLC SCL-40	Shimadzu	N/A
LS column	Miltenyi Biotec	130-042-401
BZ-X800 fluorescence microscope	Keyence	N/A

(*Continued on next page*)

Continued

REAGENT or RESOURCE	SOURCE	IDENTIFIER
LSR Fortessa X-20 cell analyzer	BD Biosciences, USA	N/A
Gel Doc EZ imager	Bio-Rad, USA	N/A
Nanodrop	Thermo Fisher, USA	N/A
A1R confocal microscope	Nikon, USA	N/A
ChemiDoc imager	Bio-Rad, USA	N/A
CFX Real-Time PCR detection	Bio-Rad, USA	N/A
BioRad pulser Xcell electroporation system	Bio-Rad, USA	N/A
NextSeq 500.	Illumina	N/A
Sysmex XP-300^{TM} Automated Hematology Analyzer	Sysmex corporation	N/A
Luminex FLEXMAP 3D multiplex system	Luminex corporation	N/A

RESOURCE AVAILABILITY

Lead contact

Further information and requests for resources and reagents should be directed to and will be fulfilled by the lead contact, Raman Bahal (raman.bahal@uconn.edu)

Materials availability

This study did not generate new unique reagents.

Data and code availability

All sequencing data has been deposited into the NCBI- Gene Expression Omnibus Database (GEO Accession number: GSE246439).

This paper does not report original code.

This article includes all data associated with the study in the accompanying tables, figures and supplementary materials. Any additional information required to reanalyse the data reported in this paper is available from the lead contact upon request.

EXPERIMENTAL MODEL AND STUDY PARTICIPANT DETAILS

Xenograft animal model

All animal experiments in this study were approved and performed in accordance with the guidelines and regulations of the Institutional Animal Care and Use Committee guidelines (IACUC A21041). Five-week-old female NOD.Cg-Prkdcscid Il2rgtm1Wjl/SzJ mice were purchased from Jackson Laboratories (USA). Mice were housed in the animal care facility at the University of Connecticut for 1 week to adapt to the environment. To generate U2932, Raji and MDA-MB-231 derived xenografts, mice were implanted with 10 million cells subcutaneously on the lower right flank. PDX mice were generated by implanting tumor fragments (diffuse large B-cell lymphoma, Patient ID 769687, specimen ID 267-B) purchased from National Cancer Institute. Tumor fragment received from NCI was split into fragments and surgically implanted using an 11-gauge trocar needle in mice. After implantation when tumors were palpable, they were randomly allocated to treatment groups and tumor size was measured daily.

Cell culture

HeLa, A549, and HEPG2 cells were cultured in EMEM and lymphoma cell lines were cultured in RPMI media (Invitrogen, USA). MDA-MB-231 was grown in L-15 media and PC3 was grown in DMEM media. Medias were supplemented with 10% FBS and 1% Penstrep and cells were maintained at 37°C and 5% CO_2.

METHODS DETAILS

Synthesis of PNA oligomers

PNAs were synthesized on MBHA (4-methylbenzhydrylamine) resin using Boc chemistry and standard solid phase synthesis protocols.[56] Regular and serine-γPNA-Boc monomers from ASM Research Chemicals (Germany) were used. Classical nuclear localization sequence (NLS; PKKKRKV) was conjugated on C terminus using Boc protected amino acids. Boc-MiniPEG3 was used as a linker and carboxytetramethylrhodamine (TAMRA) dye was conjugated on C terminus. PNAs were cleaved from the resin in trifluoracetic acid: trifluoromethane sulfonic acid: m-cresol: thioanisole at a ratio of 6:2:1:1 (v/v). Diethyl ether was used to precipitate the PNA followed by washing and vacuum drying. The crude PNAs were then purified by HPLC using 0.1% trifluoroacetic acid (TFA) in

acetonitrile and 0.1% TFA in water as mobile phases. Mass spectrometry was used to confirm the molecular weights. The purified PNAs were lyophilized and reconstituted in water and concentration was determined by measuring absorbance at 260 nm via UV-Vis spectrometry.

Gel electrophoresis

The double stranded DNA sequences (dsDNA 1 and dsDNA 2) containing the binding site for γPNA1-NLS and γPNA2-NLS were synthesized via PCR. dsDNA1 was synthesized using below primer sequences containing binding site for γPNA1-NLS.

dsDNA 1 (101 bp) primers

Forward: 5′CTCTGCTTTGGGAACCCGGGAGGGGCGCTTATGGGGAGGGTGGGGAGGG TGGGGAAGGTGGGGA 3'

Reverse: 5′AGAGTGCTCGGCTGCCCGGCTGATGTCTCTTCCCCACTCCCCACCTTCCCC ACCCTCCCCACCC 3'

dsDNA 2 was synthesized using the below primers containing the binding site for γPNA2-NLS.

dsDNA 2 (101 bp) primers

Forward: 5′TCCTGCCTCGAGAAGGGCAGGGCTTCTCAGAGGCTTGGCGGGAAAAAGA ACGGAGGGAGGGA 3'

Reverse: 5′AGATAAAGCCCCGAAAACCGGCTTTTATACTCAGCGCGATCCCTCCCTCC GTTCTTTTTCCC 3'

10x PCR reaction buffer (5 μL), 50 mM $MgCl_2$ (1.5μL), 10 mM dNTP (1 μL), 10 μM primers (1 μL each primer), and DNA Taq polymerase (0.5 μL) were mixed with water up to a volume of 50 μL. DNA was amplified in a thermal cycler using the conditions: 95°C (2 min), 95°C (30 s), 55°C (30 s), 72°C (1 min), 72°C (10 s) for a total of 10 cycles. The PCR reaction mixtures were pooled and quenched using 0.2x volume of 10 mM EDTA followed by dsDNA extraction with 1x chloroform: phenol: isoamyl alcohol (24:25:1) twice. The aqueous fractions were collected, combined and precipitated by adding 1 μL glycogen, 0.1 × 3 M sodium acetate, and 3x absolute ethanol at −20°C for 35–40 min. The precipitated dsDNA was collected by centrifugation at 15,000 RPM for 5 min, the pellet was washed with 70% ethanol twice, air-dried and reconstituted in DNase-free water. The concentration of dsDNA was measured using Nanodrop (Thermo Fisher, USA). The purified dsDNA 1 and dsDNA 2 were then incubated with different concentrations of γPNA1-NLS and γPNA2-NLS respectively in 10 mM sodium phosphate buffer at 37°C for 17 h. Samples were then separated on 10% polyacrylamide gel at 120V for 40 min. The bound and unbound fraction of dsDNA was visualized using SYBR gold staining and Gel Doc EZ imager (Bio-Rad, USA).

Cellular uptake

Confocal microscopy

HeLa cells were seeded in 8 chamber slides at 50,000 cells/well. Lymphoma cells including U2932 and Raji cells were seeded in 24 well plate at 100,000 cells per well. γPNA5-NLS-T was added to the HeLa cells at 2 μM concentration and in lymphoma cells at 8 μM. After 24 h, cells were washed with PBS to remove non-internalized PNA. The nucleus of live cells was stained using Hoechst dye and cells were visualized under confocal microscope (Nikon A1R, USA) while being maintained in CO_2 independent media. Z-stacks were captured using 2–4 μm step size and maximum intensity projection images were obtained using ImageJ 1.52a.

Florescence microscopy

MDA-MB-231 cells were seeded in a 12-well plate at 200,000 cells/well. The cells were treated with 2 μM of γPNA5-NLS-T for 24 h. After 24 h, cells were treated with colcemid (0.1 mg/ml) for 5 h. Cells were trypsinized, washed and resuspended in 75mM KCl for 20 min at 37°C. This was followed by fixing the cells using Carnoy's fixative (75% methanol and 25% acetic acid) for 10 min at 4°C. Cells were spotted on a glass slide and allowed to air dry. The nucleus was stained using ProLong Diamond Antifade Mountant with DAPI. Images were taken using a Keyence BZ-X800 fluorescence microscope (USA).

Flow cytometry

U2932 and Raji cells were treated with different γPNA5-NLS-T concentrations (1, 2, 4, and 8 μM). After 24 h, cells were collected, washed and suspended in PBS. Cells were analyzed using LSR Fortessa X-20 cell analyzer (BD Biosciences, USA) collecting 10,000 events for each sample. The data was analyzed using FlowJo 10.8.1.

PCR amplicon assay

U2932 and Raji cells were treated with PBS, γPNA2-NLS, and Scr−γPNA3-NLS at 8 μM for 24 h. U2932 cells were also treated with 0.5, 1, 2, 4, and 8 μM of γPNA2-NLS. Genomic DNA was extracted using Wizard SV genomic DNA purification kit (Promega, USA) and concentration was measured using Nanodrop. The target region containing the binding site for γPNA2-NLS was amplified using below primers:

Forward: 5′ AGGGCTTCTCAGAGGCTTG 3'

Reverse: 5′ TGCCTCTCGCTGGAATTACT 3'

200 ng of the genomic DNA from treated lymphoma cells was amplified using 2x PCR mix (25 μL) and 0.2 μM of forward and reverse primer in 50 μL volume. The target region was amplified in thermal cycler using 94°C (2 min), 94°C (30 s), 60°C (45 s), 68°C (1 min), 68°C (1 min) (40 cycles). The amplified product was purified using QIAquick PCR purification kit (Qiagen, USA). The purified amplicon (113 bp) was separated on an 3% agarose gel containing ethidium bromide for 30 min. The bands were visualized using ethidium bromide imaging application on ChemiDoc imager (Bio-Rad, USA).

γH2AX foci assay

HeLa and U2932 cells were seeded at 100,000 cells/well in a 24 well plate. Cells were treated with γPNA2 -NLS (8 μM) and bleomycin (50 and 150 μM) for 24 h. The nucleus was stained with NucBlue (ThermoFisher; #R37605) for 25 min at 37°C. Cells were then fixed with 4% paraformaldehyde (PFA) for 10 min at room temperature and permeabilized with 0.1% Triton X in PBS. Fixed cells were then incubated with anti-γH2AX antibody conjugated with phycoerythrin (PE; BioLegend; #613412) for 2 h at 37°C. Images were captured using a Keyence BZ-X800 fluorescence microscope (USA). Anti-γH2AX stained U2932 cells were analyzed on an LSR Fortessa X-20 cell (BD Biosciences, USA) flow cytometer and the data was analyzed using FlowJo 10.8.1.

Comet assay

U2932 cells were seeded in 12 well plates at a density of 200,000 cells/well. Cells were treated with γPNA2 -NLS (8 μM) and bleomycin (150 μM) for 24 h. Cells were harvested, and comet assay was performed using R&D systems CometAssay kit as per manufacturer's protocol. In brief, cells were suspended in low melting agarose at a 1:5 (v/v) ratio, added to comet slides and allowed to set at 4°C. The slides were incubated in lysis solution overnight, placed in electrophoresis solution for 30 min and then run at 21V for 45 min. The slides were kept in acetate solution for 30 min followed by 70% ethanol for 30 min. The samples were dried in a desiccator overnight, stained with SYBR gold for 30 min and visualized using a Keyence BZ-X800 fluorescence microscope (USA). The images were analyzed using CometScore 2.0.

Cell viability

U2932, Raji, Daudi cells MDA-MB-231 and PC3 were seeded in 96 well plates at a density of 20,000 cells/well. PNAs were added to the media at different concentrations (1, 2, 4, and 8 μM). After 24 h, cell viability was measured using trypan blue staining and the cell counter (Bio-Rad, USA). For testing the combination of PNAs with HDAC inhibitors, U2932 cells were pre-treated with the respective inhibitors (Valproic acid at 2 mM, Vorinostat at 2.5 μM, Romidepsin at 10 nM) for 24 h followed by addition of PNAs at 8 μM. The cell viability was then measured via trypan blue staining on days 1, 2, and 4. The cell viability was also assessed for the combination of PNAs with different concentration of chemotherapeutic drugs combination (1x CHOP dose: Cyclophosphamide at 4.1 mM, doxorubicin hydrochloride at 0.16 mM, vincristine sulfate at 0.015 mM and prednisone at 0.625 ng). U2932 cells were treated with 8 μM PNAs to sensitize the cells for 24 h. This was followed by the addition of 1x CHOP which was serially diluted at a 1:2 ratio and viability was measured by trypan blue staining after 24 h of CHOP addition.

Apoptosis assay

U2932 and Raji cells were seeded in a 12-well plate at 200,000 cells/well. The cells were treated with 8 μM of γPNA2-NLS and Scr-γPNA3-NLS for 24 h. The cells were washed with PBS and suspended in annexin V binding buffer. The cell count was measured and a 100 μL cell suspension containing $1x10^5$ cells was stained with 5 μL of FITC Annexin V and 10 μL of 7-amino-actinomycin (7AAD). After 15 h incubation in the dark, 400 μL of annexin V binding buffer was added and signal was acquired using LSR Fortessa X-20 cell analyzer (BD Biosciences, USA). A total of 10,000 events were obtained for each group and data was analyzed using FlowJo 10.8.1.

Gene expression

The levels of mRNA were measured in different cell lines using real-time PCR (RT-PCR). Total RNA was extracted using Qiagen RNeasy kit (USA) and concentration was measured using Nanodrop. cDNA was synthesized using high capacity cDNA reverse transcription kit (Applied Biosystem, USA) following the recommended cycling conditions. Taqman gene expression assay for *c-Myc* (Hs00153408), *EZH2* (Hs00544830), and *GAPDH* (Hs02758991), *BRCA2* (Hs00609073), *RAD52* (Hs01028879), *LIG4* (Hs01866071), *XRCC2* (Hs03044154), *PIF1* (Hs00228104), *CLSPN* (Hs08898637), *FANCM* (Hs00913609), *CLK1* (Hs00964634), *CLK2* (Hs02562748), *CLK4* (Hs00252917), *SRSF10* (Hs00986049), *E2F3* (Hs00605457), *BRD9* (Hs01079464), *EIF5B* (Hs01019800), *EIF4EBP* (Hs00358624), *ARL11* (Hs01936475), and *OGT* (Hs00269228) were used to amplify the respective mRNAs using the specified cycling conditions in the CFX Real-Time PCR detection system (Bio-Rad, USA). GAPDH was used as the reference gene and fold change in mRNA expression was obtained by normalizing against the untreated cells or cells treated with HDAC inhibitors.

RNA-sequencing

U2932 cells were treated with PBS or γPNA2-NLS (n = 4 replicates) at 8 μM for 48 h and 72 h. Cells were also transfected with siRNA targeting the *c-Myc* mRNA (Invitrogen, #VHS40785) using electroporation. In brief, 500 nM of siRNA was mixed with 5×10^6 U2932 cells in a 4 mm cuvette and pulsed once using 316V and 500μF using BioRad pulser Xcell electroporation system. Total RNA was extracted after 48 h. Total RNA was extracted from the collected cell pellets and submitted for RNA sequencing analysis. Illumina TruSeq stranded total RNA and mRNA was used for library preparation. The samples were then sequenced using Illumina NextSeq 500. All downstream analyses were accomplished by R (4.0.4). Differentially expressed genes (DEGs) between different groups were identified by the package DESeq2 (1.30.1) with a filtering criterion of $\log_2$ (fold change) > 0.5 and padj<0.05.[101] Samples treated for 72 h were used to identify to identify specific pathways overrepresented in the DEGs. The package clusterProfiler (3.18.1) was used and significant pathways were picked out by setting p value cutoff = 0.05 and qvalue cutoff = 0.05.[102] The protein-protein

interaction (PPI) analysis was performed with a confidence cutoff of 0.4 using search tool for retrieval of interacting genes/proteins (STRING) database in cytoscape 3.9.1. Samples treated for 48 h were used for GSEA analysis. Batch correction of raw RNA-seq expression matrix was done by the function ComBat in the package sva (3.46.0), and this corrected matrix was used in heatmap plot and GSEA. c-Myc target gene sets were downloaded from the GSEA website (https://www.gsea-msigdb.org/gsea/index.jsp). GSEA (Linux_4.1.0) software was utilized to determine whether these gene sets showed statistically significant difference between different groups. NES and nominal p values of well characterized MYC signature gene set were calculated from technical replicates.

In vivo studies in xenograft mice model

U2932, Raji and MDA-MB-231 derived xenografts were generated by implanting 10 million cells subcutaneously on the lower right flank of the female NSG mice (NOD.Cg-Prkdcscid Il2rgtm1Wjl/SzJ, #005557, Jackson Laboratories, USA) of about 5–6 weeks age. The mice were maintained in the animal care facility at the University of Connecticut following the required Institutional Animal Care and Use Committee guidelines (IACUC). Mice developed palpable U2932 tumors after 3–4 weeks and Raji xenografts after 2–3 weeks of implantation. Tumor dimensions including length (L), breadth (b), and height (h) were measured using a caliper and volume was calculated using the formula for ellipsoid (0.5236×lbh).

Biodistribution studies

Mice with 600–800 mm^3 U2932 tumor volume were used for the biodistribution studies. γPNA5-NLS-T was injected systemically (retro-orbital) at 5 mg/kg dose. Live imaging of animals was performed using *in vivo* imaging (IVIS) spectrum CT and epifluorescence was recorded at excitation/emission wavelength of 535/580 nm at 0, 0.25, 1, 2, 4, 6, 8 and 24 h. Mice were euthanized after 6 and 24 h. Organs were collected and imaged via IVIS to determine the localization of γPNA5-NLS-T. Later, organs were frozen in optimum cutting temperature media (OCT) at −80°C. The tumor, liver, and kidney from treated and untreated mice were sectioned using a cryostat to obtain 10 μm tissue sections. The sections were washed in PBS followed by fixation in 10% neutral buffered formalin. After washing with PBS, sections were permeabilized using 0.2% Triton X-100. The nucleus was stained using mounting media with DAPI (Invitrogen, USA). Sections were allowed to harden overnight, and images were taken using 60x oil lens on a Nikon A1R confocal microscope (USA).

Short-term efficacy

The mice were treated when the tumors reached a volume of 600–800 mm^3 for U2932 xenografts and 400–500 mm^3 in Raji xenografts. γPNA2-NLS was administered systemically at 25 mg/kg in U2932 xenograft mice. Raji xenografts were treated with γPNA2-NLS at 5 mg/kg via intra-tumoral route. After 24 h, mice were euthanized, and tumors were dissociated and used for Western blot analysis.

Survival study

Mice bearing tumors about 100–150 mm^3 were divided into 3 groups. Mice were treated with either saline (n = 10), γPNA2-NLS (n = 9), or Scr-γPNA3-NLS (n = 8). PNAs were administered at 5 mg/kg dose on days 1, 4, 7, and 10. A second study with mice bearing tumors 100–150 mm^3 was conducted to access the effect of combination treatment. Mice were divided into 6 groups: romidepsin (n = 8), γPNA2-NLS + romidepsin (n = 8), vehicle (n = 5), and CHOP (n = 7), γPNA2-NLS + CHOP (n = 8), control (n = 6). Romidepsin was administered intraperitoneally at 1 mg/kg on days 0 and 6. γPNA2-NLS was administered at 5 mg/kg on days 1, 4, 7 and 10. 1x dose of CHOP (Cyclophosphamide at 2.5 mg/kg, doxorubicin hydrochloride at 0.2 mg/kg, vincristine sulfate at 0.03 mg/kg and prednisone at 0.0125 mg/kg) was administered on day 1 and 3x dose of CHOP was administered on days 7 and 13. γPNA2-NLS for the CHOP combination treatment was administered at 5 mg/kg on days 0, 3, 6 and 9. The change in tumor volume and body weight was measured every day. Mice were euthanized when the tumor volume reached 2000 mm^3. Blood was collected via cardiac puncture in 1.5 mL tubes containing 0.5 M EDTA. Organs including tumor, liver, kidney, spleen, heart and lung were collected. Tumor fractions and all organs were kept in 10% formalin and submitted for histology. The complete blood count (CBC) analysis was performed on the collected blood samples using Sysmex CBC analyzer (USA). Plasma was separated from the blood samples and submitted to Antech diagnostic for blood chemistry analysis to quantify the levels of alanine transaminase (ALT), lactate dehydrogenase (LDH), aspartate transaminase (AST) and blood urea nitrogen (BUN).

Tumor dissociation

The collected tumor fragments from short term study and survival study were processed to enrich the implanted human tumor cells. The tumor fragments were chopped into small fragments under sterile conditions and dissociated using dispase (Stem cell technologies, #100–0396), collagenase (Worthington, #LS004194) and RPMI media at 37°C for 1.5 h. The dissociated tumor fragments were centrifuged, washed with PBS, and passed through a 70-micron filter. The collected single cell suspension of tumor cells was centrifuged and incubated with 1 mL trypsin for 5 min at RT. Cells were then diluted in RPMI media and passed through a 40-micron filter. The collected cells were centrifuged and resuspended in 0.5–0.7 mL of RBC lysis buffer at RT for 4 min. Cells were then diluted in PBS and centrifuged. The obtained tumor cell pellet was suspended in 0.5% BSA and cell count was determined. To enrich the human tumor cells, 2×10^7 live cells were incubated with 20 μL of mouse cell depletion cocktail (Miltenyi Biotec, #130-104-694) at 4°C in dark for 15 min. Cell suspension was then diluted to 0.5 mL using 0.5% BSA and passed through the LS column (Miltenyi Biotec, #130-042-401). The collected cells were the enriched human tumor cells. Cells were centrifuged and pellets were stored at −80°C for further analyses.

In vivo studies in PDX mice

PDX tumor fragments (diffuse large B-cell lymphoma, Patient ID 769687, specimen ID 267-B) were purchased from National Cancer Institute. PDX mice were generated by implanting tumor fragments subcutaneously on the lower right flank of 4–6 weeks old male NSG mice (NOD.Cg-Prkdcscid Il2rgtm1Wjl/SzJ, #005557, Jackson Laboratories, USA). Tumor fragment received from NCI was split into 5 fragments and surgically implanted using an 11-gauge trocar needle in 5 mice. The mice were regularly monitored and PDX tumors were collected when the volume reached ~1500 mm^3. The PDX tumors were then implanted again in 38 mice using the same procedure. The mice were divided into 6 groups once the tumor volume reached 100–150 mm^3: γPNA2-NLS (n = 6), romidepsin (n = 6), γPNA2-NLS + romidepsin (n = 6), CHOP (n = 6), γPNA2-NLS + CHOP (n = 5) and control (n = 9). The dosage regimen of romidepsin, CHOP and γPNA2-NLS was kept similar to the one used for U2932 xenograft study. The change in mice weight and tumor volume was measured every day. Mice were euthanized when the tumor volume reached 1800–2000 mm^3. Blood and organs were collected and processed in the same manner as mentioned in U2932 xenograft mice survival study.

In vivo studies in transgenic mice model

Eμ-myc mice model of Burkitt's lymphoma (B6.Cg-Tg(IgHMyc)22Bri/J, #002728, Jackson laboratories) was used to test the efficacy of the designed PNA-NLS.

Biodistribution study

γPNA-NLS-T was administered via retro-orbital and subcutaneous route at 5 mg/kg dose in mice with visibly enlarged lymph nodes (cervical, brachial, axillary, and inguinal). Mice were euthanized after 24 h and organs were collected followed by imaging via IVIS. All major organs and enlarged lymph nodes were collected and frozen in OCT media. The lymph nodes and organs were sectioned at 10 μm thickness using cryostat. The sections were then fixed, permeabilized, and nucleus was stained with DAPI. The localization of PNA in lymph nodes was studied via confocal microscopy. Images were taken using 60x oil lens on an A1R confocal microscope (USA).

Efficacy study

Eμ-myc mice (mixed male and female) with visibly enlarged lymph nodes were divided into two groups. Mice were treated with γPNA4-NLS subcutaneously at 60 mg/kg dose over 2 days. Mice were euthanized on day 3 followed by collection of major organs and lymph nodes. Organs and sections of lymph nodes were fixed in formalin for histology. Blood was collected via cardiac puncture in 1.5 mL tubes containing 0.5 M EDTA and plasma was separated. Plasma samples were submitted to UConn Health for multiplex analysis of cytokines using the R&D systems mouse Luminex assay. Customized Luminex premade plates were obtained to screen for: TNFα, MCP-1, IL-1β, IL-4, IL-5, IL-6, IL-17A, IL-3, MIP-1α, IL-1α, MIP-1β, IL-25. Data was acquired on a calibrated Luminex FLEXMAP 3D multiplex system. Lymph nodes were further processed into single cell suspension by mashing them and passing through the 40 μm filter in RPMI media. Cells were suspended in RBC lysis buffer for 2 min followed by washing with PBS. Single cell suspension was then collected for protein analysis.

Immunotoxicology studies

Cytokine array analysis

Plasma samples were analyzed from two mice models: Eμ-myc mice and C57BL/6J mice which were treated with 60 mg/kg (subcutaneous) and 25 mg/kg (IV) of γPNA2-NLS respectively. After treatment, mice were euthanized. Blood was collected via cardiac puncture in 1.5 mL tubes containing 0.5 M EDTA and plasma was separated. Plasma samples were submitted to UConn Health for multiplex analysis of cytokines using the R&D systems mouse Luminex assay. Customized Luminex premade plates were obtained to screen for: TNFα, MCP-1, IL-1β, IL-4, IL-5, IL-6, IL-17A, IL-3, MIP-1α, IL-1α, MIP-1β, IL-25. Data was acquired on a calibrated Luminex FLEXMAP 3D multiplex system.

Immune cell composition

C57BL/6J mice were treated with a dose of 25 mg/kg dose of γPNA2-NLS systemically (retro-orbital). After 24 h, mice were euthanized and blood was collected via cardiac puncture. RBCs from 500 μL blood were lysed using 5mL of eBioscience 1x RBC lysis buffer. The cells were centrifuged and washed with 1x phosphate buffered saline (PBS) and were stained with LIVE/DEAD Fixable Aqua Dead (Thermo Fisher, #L34957) for 20 min at room temperature, to exclude dead cells. This was followed by staining with appropriate surface makers (Table S2) for 30 min at 4°C. Cells were fixed with 4% paraformaldehyde for 10 min at 4°C. This was followed by washing, and resuspension in 1x PBS. Samples were acquired on an LSR Fortessa X-20 (BD Biosciences, USA) flow cytometer collecting 100,000 events for each sample. The gating strategy is shown in Figure S7H. Percentages of various cell subsets were compared with C57BL/6J mice treated with saline. The data was analyzed using FlowJo 10.8.1.

Monocyte uptake study

C57BL/6J mice were treated with a dose of 5 mg/kg dose of γPNA5-NLS-T systemically. After 24 h, mice were euthanized and blood was collected via cardiac puncture. Blood cells were processed and analyzed in the same method described in immune cell composition section. The surface markers used to identify the monocyte population were CD11b and F4/80. C57BL/6J mice treated with saline were used as control. The data was analyzed using FlowJo 10.8.1.

Western blot analysis

Total protein was extracted from cell pellets, enriched human tumor cells, and lymphocytes using 1x RIPA buffer (Cell signaling technology, USA) containing protease inhibitor. The concentration of protein was determined using absorbance-based DC protein assay (Bio-Rad, USA). Equal amount of protein (25–40 μg) was separated on a 4–20% SDS-PAGE gel followed by transfer to the PVDF membrane. c-MYC(Cell signaling technology (CST), #5605), EZH2 (CST, #5246), γH2AX (CST, #9718S) proteins were probed using rabbit monoclonal primary antibody in 3% BSA at 4°C overnight. Cyclophilin B (CST, #43603) and β-actin (CST, #4970) were probed as the endogenous controls. The bands were detected using anti-rabbit IgG HRP linked secondary antibody (Cell signaling technology, #7074) (1:2000 dilution, 5% milk in Tris-buffered saline containing 0.1% Tween 20) and HRP substrate (Millipore sigma, USA). The blots were imaged using ChemiDoc imager (Bio-Rad, USA) and band intensities were quantified using ImageJ 1.52a and cyclophilin B as a loading control.

Immunohistochemistry

Four-micron tissue sections were obtained from paraffin-embedded blocks. Dewaxing was performed by heating the slides at 60°C for 15 min in a hot air oven. Tissue sections were then deparaffinized in xylene for 10 min, followed by hydration with sequential dipping of sections in 100-75% ethanol. Antigen retrieval was performed using the low pH antigen retrieval buffer (Thermo Fisher, #00-4956-58) in a steamer for 1 h at 95°C. After each of the following steps, the sections were washed with phosphate-buffered saline containing 0.05% Tween 20 (PBST). Blocking was performed using 2.5% normal horse serum for 30 min at room temperature. The primary antibodies for Ki-67 (clone D2H10; 9027S) and caspase 3 (clone D3R6Y; 14214S) staining were purchased from CST and were incubated at a 1:200 dilution at room temperature for 2 h. This was followed by peroxidase blocking (3% H_2O_2) for 10 min at room temperature. The sections were then incubated with the ImPRESS HRP–polymer horse anti-rabbit secondary antibody (Vector laboratories; MP-7401) for 30 min at room temperature. The 3,3′-diaminobenzidine (DAB) (Vector laboratories; SK4100) solution was freshly prepared and added to each section for 3–5 min followed by washing in PBST. The sections were counterstained with hematoxylin for 30 s and mounted using DPX mounting media (Electron Microscopy Sciences, #13510). The slides were imaged on a Keyence BZ-X800 microscope (USA) and DAB intensity was quantified using ImageJ 1.52a. The results are plotted to include all data points ($n = 2$ independent mice in each group, and $n > 4$ images were quantified per tumor section).

Statistical analysis

GraphPad Prism 9 (version 9.4.1) was used for statistical analysis. The data were reported as mean ± SEM and the number of replicates are included in the figure captions. An unpaired two-tailed t-test was performed for experiments to test significance between the two groups. Two-way ANOVA was performed to test statistically significant differences between multiple groups.